Tacr1 marks a population of long-range inhibitory neurons that regulate neurovascular coupling

by

Catherine Faber Ruff

B.S., University of Iowa, 2004

M.S., Cornell University, 2009

D.V.M., Purdue University, 2013

Submitted to the Graduate Faculty of the

School of Medicine in partial fulfillment

of the requirements for the degree of

Doctor of Philosophy

University of Pittsburgh

2021

UNIVERSITY OF PITTSBURGH

SCHOOL OF MEDICINE

This dissertation was presented

by

Catherine Faber Ruff

It was defended on

March 30, 2021

and approved by

Kenneth N. Fish Associate Professor, Department of Psychiatry

Bryan M. Hooks, Assistant Professor, Department of Neurobiology

Caroline Runyan, Assistant Professor, Department of Neuroscience

Edith Hamel, Professor, Department of Neurology and Neurosurgery

Sarah E. Ross Academic Associate Professor, Department of Neurobiology

Dissertation Director: Alberto L. Vazquez, Research Associate Professor, Department of Radiology and Bioengineering

***Tacr1* marks a population of long-range inhibitory neurons that regulate neurovascular coupling**
Catherine Faber Ruff, PhD

University of Pittsburgh, 2021

The brain is a metabolically expensive organ consuming 20% of the body's energy at rest yet lacks energy reserves. To meet the high energy demands of active neurons blood flow parallels changes in brain activity by a mechanism known as neurovascular coupling (NVC). Although this mechanism is critical to normal brain function and the basis of functional brain imaging, a standard modality for measuring neural activity in health and disease, NVC is incredibly complex and the process remains poorly understood. Here, we identify a unique population of cortical GABAergic that express a G-protein coupled receptor, tachykinin receptor 1 (*Tacr1*), in mouse and humans. Whole-tissue clearing experiments reveal that these *Tacr1* neurons extend local and long-range projections across functionally connected cortical regions. Through two-photon microscopy and calcium imaging, we show that whisker stimulation drives activity in *Tacr1* neurons in the barrel cortex. Tacr1 neurons receive direct excitatory drive from both glutamatergic thalamocortical and corticocortical neurons shown by subcellular ChR2-assisted circuit mapping. Optogenetic activation of *Tacr1* neurons in vivo is sufficient for vasodilation, whereas ArchT-mediated inhibition of these cells significantly reduces the whisker-evoked hemodynamic response. Furthermore, vasodilation mediated by *Tacr1* neurons is initiated by capillary pericytes. Finally, by electron microscopy we see that *Tacr1* presynaptic terminals and postsynaptic densities contact astrocytes. These findings identify a neural correlate that integrates cortical activity to modulate cerebral blood flow.

Table of Contents

List of Figures

1.0 Introduction

The brain's dependence on blood flow is unlike any other organ in the body. If cerebral blood flow (CBF) is interrupted, brain function ceases within seconds and there is irreversible damage to neurons within minutes (Hall and Hall 2021b). Most tissues of the body can live without oxygen for several minutes or longer, but the brain's lack of fuel reserves and the high metabolic demands of active neurons require a continuous, second-to-second, flow of blood to maintain brain health. To meet these demands, several mechanisms have developed to ensure that there is a continuous flow of nutrient-rich blood to the brain.

1.1 Cerebral blood flow (auto)regulation

Cerebral blood flow (CBF) regulation is a homeostatic process that regulates and maintains a constant cerebral blood flow (CBF) across a range of arterial blood pressures (Hall and Hall 2021a). Cerebral blood flow (CBF) is defined as the ratio between cerebral perfusion pressure (CPP) and cerebral vascular resistance (CVR) and is based on Ohm's law (Fig. 1) (Uludag et al. 2004). Cerebral blood flow regulation is largely achieved by regulating the resistance of vessels in the brain, which is accomplished most effectively by modulating the diameter of arteries and arterioles (Peterson, Wang, and Britz 2011). There are normal changes in mean arterial pressure (MAP) throughout a day, which range from small, such as those associated with a posture change (i.e., standing up), to large, such as those that occur with strenuous exercise. Regardless of the magnitude, CBF regulation prohibits elevations in MAP from affecting the cerebral blood pressure

$$CBF = \frac{CPP}{CVR} = \frac{MAP - ICP}{CVR}$$

Figure 1 | Equation for the calculation of cerebral blood flow

The general equation for cerebral blood (CBF) is based on Ohm's law. Ohm's law defines current flow as voltage divided by resistance. In CBF terms, Ohm's law is adapted and (cerebral) blood flow is expressed as a ratio between cerebral perfusion pressure (CPP) and cerebral vascular resistance (CVR). CPP is difference between mean arterial pressure (MAP) and intracranial pressure (ICP).

by narrowing the diameter of vessels. Conversely, a decrease in MAP tends to decrease CBF, and the CBF regulation cause vessels to dilate to equalize CBF. Because conductance in a vessel increases in proportion to the fourth power of the vessel diameter, slight changes in diameter can cause tremendous changes in the vessel's ability to conduct blood (Hall and Hall 2021b). For example, a 4-fold increase in vessel diameter can increase blood flow as much as 256-fold (Fig. 2a). Interestingly, this fourth power law makes it possible for small changes in the diameter of arterioles and capillaries (although debatable) to have a profound impact on blood flow.

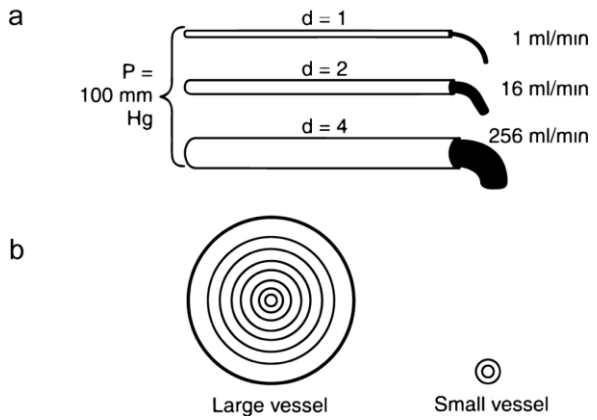

Figure 2 | Vessel conductance is proportion to the fourth-power of the vessel diameter

a, Schematic depicting three vessels with relative diameters of 1, 2, and 4. Pressure is constant at 100 mm Hg. The diameters of the vessels increase fourfold; however, their respective flows are 1, 16, and 256 ml/min. The conductance of a vessel increases in proportion to the fourth-power of the diameter: conductance $\propto$ diameter^4. **b**, Cross section of a representative large and small vessel depicting laminar flow - blood closer to the vessel wall adheres to the vascular endothelium and is slowed, whereas blood in the center of the lumen flows more rapidly. The concentric rings inside the vessels indicate arbitarily different velocities. Schematic adapted from Hall & Hall, 2021.

The regulatory response of the cerebrovascular system to arterial pressure fluctuations only occurs if CBF regulation is working properly. In pathological conditions where CBF regulation is impaired or absent, CBF is no longer maintained at a steady state, but parallels fluctuations in mean arterial blood pressure. Therefore, in diseases associated with CBF dysregulation, such as Alzheimer's Disease (AD), increases in mean arterial pressure would also cause an increase in cerebral perfusion pressure and a subsequent increase in CBF. Unregulated increases in CBF can cause vessels to rupture, leading to hemorrhages in the brain. Moreover, chronic CBF dysregulation can be catastrophic leading to cerebral stroke (Xiao et al. 2017).

1.1.1 Mechanisms of CBF regulation

CBF autoregulation is essential, maintaining a constant CBF despite increases in systemic blood pressure, but the mechanisms of CBF regulation is complex and only partially understood. It is generally accepted that the regulatory mechanism is multimodal, consisting of myogenic, metabolic, endothelial and neurogenic processes (Uludag et al. 2004; Hall and Hall 2021a). The myogenic mechanism involves vascular smooth muscle cells contracting in response to increased blood pressure. The transmural pressure change activates mechanically sensitive ion channels in vascular smooth muscle cells, triggering downstream cascades that ultimately lead to an influx of calcium in the cells and vasoconstriction (Cipolla 2009). In the metabolic mechanism, molecules that are believed to contribute to CBF regulation include carbon dioxide (CO^2), hydrogen (H^+) and oxygen (O_2) concentrations. These molecules are either directly vasoactive or produce metabolic intermediates that directly cause smooth muscle vasodilation (Armstead 2016). For example, CO_2 combines with water to form carbonic acid, which dissociates from the acid to form H^+. Hydrogen ions directly cause vasodilation in cerebral vessels, and the dilation is almost directly proportional to the H^+ concentration. Likewise, the endothelium releases a variety of vasoactive substances that affects vessel tone in the brain. Interestingly, hydroxymethylglutaryl (HMG)-CoA reductase inhibitors, or statins, have been associated with improved stroke outcome (Giannopoulos et al. 2012). The effect of statins on CBF regulation is mediated mainly through the upregulation of endothelium nitric oxide synthase (eNOS), thus an increase in the bioavailability of a nitric oxide (NO), a potent vasodilator.

Lastly, the neurogenic response of CBF regulation includes the effects of the autonomic nervous system and a mechanism known as neurovascular coupling. Extra-parenchymal pial

arteries and arterioles contain perivascular nerves within their adventitial layer that are associated with the sympathetic and/or the parasympathetic nervous system. These perivascular neurons associated with the autonomic nervous system can directly affect vessels, but their contribution to CBF regulation is unclear. The main neurogenic response of CBF regulation is neurovascular coupling (NVC) which is a rapid local increase in blood flow to an active brain region. It is generally accepted that this mechanism is driven by neurotransmitter-related signaling, but how neurons communicate their energy needs to blood vessels is not completely understood.

1.2 Neurovascular coupling

Roy and Sherrington's feed-back mechanism for cerebral blood flow regulation proposed that oxygen demands were signaled by vasoactive metabolites originating from neurons (Zhang et al. 2020; Nair 2005; Iadecola 2017). This mechanism was supported by early studies demonstrating that increases in CBF matched local tissue oxygen consumption. This feed-back mechanism of CBF regulation was generally accepted until the development of functional magnetic resonance imaging (fMRI) in the mid1980s. Blood oxygenation level dependent (BOLD) fMRI studies showed a mismatch between increases in blood flow and the metabolic rate of oxygen (Fox and Raichle 1986; Raichile 1998; Nielsen and Lauritzen 2001). Moreover, concurrent electrophysiology and fMRI recordings found that with increased neuronal activity, cerebral blood flow increases substantially, while cerebral metabolic rate of oxygen ($CMRO_2$) increases only moderately (Fox and Raichle 1986). In areas of functional activation, the CBF response is 6–10 times greater than the increase in $CMRO_2$ (Uludag et al. 2004; Hoge et al. 1999). Together, this non-reciprocal relationship between blood flow and oxygen metabolism suggested that CBF is

regulated by factors other than metabolic byproducts indicating a demand for oxygen (Hoge et al. 1999). Furthermore, CBF showed to be a better predictor of neural activity and paralleled neural activity both temporally and spatially. Based on this work using BOLD fMRI, a feed-forward neurovascular coupling mechanism was proposed. In this mechanism, CBF responses are driven by neurotransmitter-related signaling and not directly (or completely) by the local metabolic needs of neurons. It is now believed to be primarily driven by the CBF response, instead of oxygen metabolism, as a (indirect) measurement of neural activity in BOLD fMRI imaging. Intriguingly, this raised the question of what the neural signal is, or how do neurons communicate with the vasculature to trigger a CBF response.

1.3 Cerebral vasculature and the neurovascular unit

The brain is a highly vascularized organ consisting of a vascular network extending approximately 400 miles (~644 km) in length (Sweeney et al. 2018). On the surface of the cortex there are pial arteries and arterioles. These vessels are lined by a single layer of endothelial cells, bordered by several layers of smooth muscles cells. Loose interstitial connective tissue (adventitia) surrounds the smooth muscle cell layer (tunica media) and contains smaller vessels and nerve bundles originating from superior cervical, sphenopalatine and trigeminal ganglia (Attwell et al., 2010). Peripheral to the adventitia is the perivascular Virchow-Robin space. This perivascular space represents a modified invagination of the leptomeninges that continuous with the subarachnoid space and filled with cerebrospinal fluid (Grant, Maxie et al., 2016). In normal conditions, this space appears nonexistent, especially around intra-parenachymal capillaries. In

inflammatory or neoplastic conditions, these spaces become pronounced as it fills with invading neoplastic or inflammatory cells.

As pial arteries dive into the neuroparenchyma, the composition of the vessel is modified in both diameter and cellular composition. Most obvious is the narrowing and branching of arteries into arterioles and capillaries. In addition, the tunica media, or smooth muscle cell layer, is also reduced, measuring approximately 1-3 smooth muscle cells thick. Currently, it is not clear if some of these neural projections directly contact microvessels and astrocytes, or if NVC mediators reach their target by diffusion. The vessels are composed of a single layer of endothelium that are interconnected by tight junctions and form the foundation of the blood-brain barrier. Endothelial cells are surround by a layer of smooth muscle cells that vary in cell thickness, morphology and protein expression as vessels transition from arterioles to capillaries (Grant et al. 2019). Astrocytes project their terminal processes, or endfeet, onto smooth muscle cells which are connected by to each other by tight junctions (Iadecola, 2017). Collectively, the endothelium, smooth muscle cells and astrocytes make up the neurovascular unit.

1.3.1 Mechanisms of neurovascular coupling

Generally, neurovascular coupling starts when there is an increase in neural activity and ends with vessel dilation and a subsequent local increase in blood flow. This mechanism requires that an electrical neural signal be translated into a hemodynamic response, but how neurons communicate their energy needs to blood vessels is only partially understood.

1.3.1.1 Neurons

Various pharmacology studies have reported that glutamate receptor activation is necessary for the full expression of the sensory-evoked CBF response (Zonta et al., 2003). Additionally, c-Fos activity mapping paired with double immunohistochemistry found that cyclooxygenase 2 (COX-2)- expressing pyramidal neurons contribute to sensory-evoked CBF (Lecrux et al. 2011; Vaucher, Linville, and Hamel 1997). Consistent with this, single-cell RNA sequencing studies demonstrated that COX-2 is expressed in excitatory neurons and recent optogenetic experiments have shown that activation of excitatory neurons is sufficient for increased local blood flow (Lee et al. 2020; Tasic et al. 2016). It is generally accepted that the mechanism of excitatory-evoked NVC is mediated by prostaglandin E2 (PGE_2) although it is controversial whether or not prostaglandin receptors, E2 and EP4, exist on vascular smooth muscle cells (Lacroix et al. 2015; Kaplan, Chow, and Gu 2020; Tasic et al. 2016).

There is a large body of circumstantial evidence highlighting the importance of gamma aminobutyric acid (GABA) -ergic neurons in neurovascular coupling, either through the release of specific mediators (including neurotransmitters, neuromodulators or neuropeptides), or through the modulation of excitatory neurons (Anenberg et al. 2015; Uhlirova et al. 2016; Cauli et al. 2004; Echagarruga et al. 2020; Krawchuk et al. 2019; Shen et al. 2019; Krawchuk et al. 2020). In addition, reports of the unique proximity of GABAergic neurons to blood vessels (< 15 um) and their expression of vasoactive mediators also suggest a potential role in NVC (Vaucher et al. 2000; Tong and Hamel 2000; Iadecola et al. 1993). In acute cortical slices, stimulation of cholinoceptive or serotoniceptive vasointestinal peptide (VIP) and neuronal nitric oxide synthase (NOS) interneurons induced vasodilation, whereas Sst interneurons elicited vasoconstriction (Cauli et al.

2004). NPY interneurons, by triggering vasoconstriction, may be responsible for the post-stimulus undershoot of sensory-evoked CBF (Uhlirova et al. 2016). In addition, activation of parvalbumin interneurons in the dentate gyrus induced NO-mediated vasodilation and neurogenesis in young animals (Shen et al. 2019). Altogether, these studies point to an unequivocal role of cortical interneurons in driving the hemodynamic response.

1.3.1.1.1 nNOS GABAergic neurons

Many groups have postulated that NVC is regulated by NO (Lourenco et al. 2017; Cauli et al. 2004; Echagarruga et al. 2020; Duchemin et al. 2012; Munoz, Puebla, and Figueroa 2015; Vaucher et al. 2000; Krawchuk et al. 2019; Iadecola 1993). NO is a potent vasodilator and gaseous signaling molecule that is present in most tissues. Nitric oxide synthase (NOS) catalyzes the formation NO from L-arginine (Olesen, 2008). There are three NOS isoforms: endothelial NOS (eNOS), neuronal NOS (nNOS) and inducible NOS (iNOS). nNOS is found in both central and peripheral neurons whereas eNOS is present in vascular endothelium. iNOS is not normally detectable, but it can be induced by stimuli unrelated to intracellular calcium. Cortical nNOS neurons are divided into two subtypes, Type I and Type II, based on morphology and dihydronicotinamide adenine dinucleotide phosphate diaphorase (NADPH-D) staining intensity (Perrenoud et al. 2012; Dittrich et al. 2012). Type I nNOS neurons express higher levels of nNOS and uniquely co-express the tackykinin receptor 1 in all species evaluated (mice, rats and nonhuman primates) (Dittrich et al. 2012). Tacr1 inhibitory neurons are a small population, representing approximately 2% of total interneurons in the cortex (Dittrich et al. 2012). These neurons are concentrated in layers 5/6, and they are thought to send long-range intracortical

projections. These features make Tacr1 neurons ideally poised to modulate blood flow (He et al. 2016).

1.3.1.1.1.1 Nitric oxide-mediated neurovascular coupling

Although early studies showed normal CBF in animals despite a loss of Nos1, more recent work, including work done by our group, suggests an unequivocal role of nitric oxide, and more specifically Nos1-expressing neurons in NVC (Shen et al. 2019; Echagarruga et al. 2020; Lourenco et al. 2014; Vazquez, Fukuda, and Kim 2018). The reasons for the contradictory findings in early studies are twofold: first, compensatory mechanisms likely restored any deficits in NVC in the global knockout animal models used, and second, CBF was evaluated in animals under anesthesia. In addition, initial analysis of nNOS mutant mice suggested a complete absence of nNOS protein and mRNA in brain and peripheral tissues. However, residual NOS catalytic activity was detected in brain at levels up to 8% of that found in wild-type animals (Huang et al. 1993). Interestingly, more recent work in awake mice using acute short interfering RNA- mediated knockdown of Nos1 in the hippocampus show substantially reduced NVC.

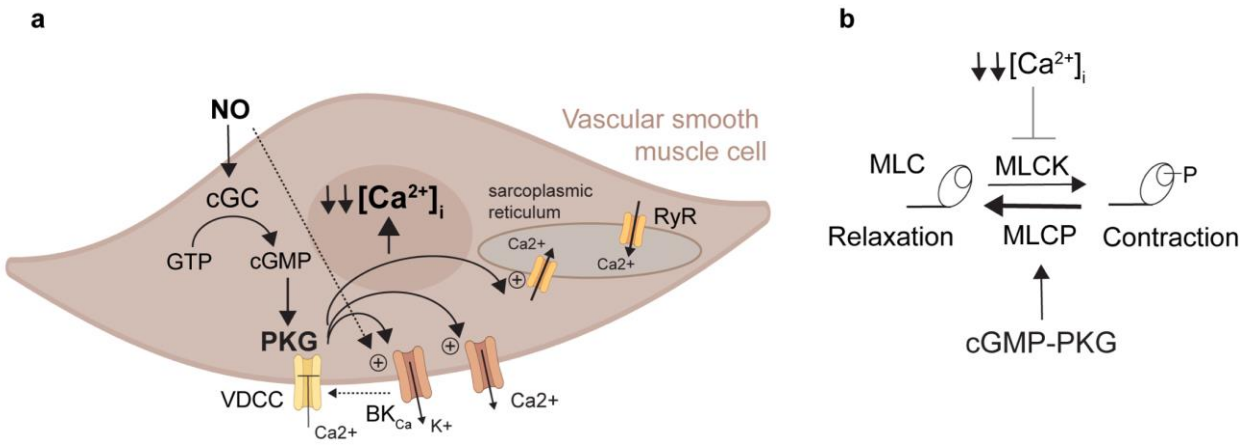

Figure 3 | Nitric oxide-mediated smooth muscle cell relaxation

Schematic depicting NO-cGMP mediated VSMC relaxation pathway. **a**, Nitric oxide (NO) enters VSMC, and activates soluble guanylate cyclase (sGC) and converting GTP to cGMP. cGMP activates cGMP-dependent protein kinase (PKG). Activated PKG phosphorylates key target proteins including Ca^{2+}-activated K^+ (BK_{Ca}) channels, L-type voltage-gated Ca^{2+} channels (VDCC), sarcolemma Ca^{2+}/ATPase pump (ryanodine receptors, RyRs) and myosin light chain phosphatase (MLCP) inhibitor. Activation of BK_{Ca}, increases K efflux inhibits Ca^{2+} influx via VDCC **b**, PKG and PKG-mediated decrease in intracellular Ca^{2+} concentration ($[Ca^{2+}]_i$) relaxes VSMCs. Note, not all known PKG targets are included in schematic.

Nitric oxide mediates smooth muscle relaxation via cyclic (cGMP)-dependent protein kinase (PKG) signaling pathway (Fig. 3a). NO diffuses in smooth muscle cells and activates soluble guanylate cyclase (s-GC), a cytosolic enzyme that converts guanosine triphosphate (GTP) to cGMP (Carvajal et al. 2000; Yang et al. 2005). cGMP is considered the main mediator of the cellular effects produced by NO and activates cGMP-dependent protein kinase (PKG). The binding and activation of cGMP-dependent protein kinase (PKG) is responsible for most of the intracellular actions of cGMP and reduces cytosolic Ca^{2+} through a number of complexes and partially understood mechanisms (Carvajal et al. 2000). Briefly, PKG activates of Ca^{2+}-activated K (BK_{Ca}) channels and ryanodine receptors (RyRs), reducing intracellular Ca^{2+} concentrations and

subsequent hyperpolarization. In addition, PKG phosphorylates the myosin light chain phosphatase (MLCP) inhibitor (Fig. 3b). The contractile state of VSMCs is mainly determined by the phosphorylation level of myosin light chains (MLC) (Duchemin et al. 2012). A net decrease in MLC phosphorylation results in VSMC relaxation.

2.0 Methods

2.1 Experimental Animals

All animals were cared for in compliance with the National Institutes of Health guidelines and approved by the University of Pittsburgh Institutional Animal Care and Use Committee. Previously generated *Tacr1*^{creER} mice (ref. (Huang et al. 2016); referred to as *NK1R*^{creER} mice) were bred in house and maintained on a C57BL/6 background. The following mice strains were used: wild type (C57BL/6J, Charles River, no. 027), *NG2*^{creER} (ref. (Hartmann et al. 2015), JAX, no. 008538), Ai9 (JAX, no. 007909), Ai32 (JAX, no. 012569), Ai35 (ref. (Madisen et al. 2012); JAX, no. 012735), Ai95 (JAX, no. 028865), Vip-Flp (JAX, no. 028578). All mice were maintained on a C57BL/6J background and both males and females were used. For mice expressing *CreER*, tamoxifen (Sigma-Aldrich, T5648) was dissolved in corn oil at a concentration of 20 mg ml^{-1} and injected into peritoneal cavities at a dose 75 mg kg-^{1}. Mice that were bred to a reporter or used for electrophysiology experiments were treated with tamoxifen for five consecutive days or every other day if body weight decreased by 10% or more. Mice receiving an intracranial Cre-dependent adenovirus (AAV) were treated with tamoxifen starting two days post-surgery. Animals recovered for at least one week following the last tamoxifen treatment before cranial surgery or dissections were performed. Randomization was determined by mouse genetics as wild types, mutants and transgenic mice were assigned randomly into their respective genotype group. Sample sizes were determined by a power calculation based on previous pilot data and representative sample sizes from previous literature that had similar experiments. Investigators were not blinded to the genotypes during data acquisition and analysis.

2.2 Immunohistochemistry

After anesthesia tamoxifen-treated Tacr1creER-tdT (Ai9) adult mice were transcardially perfused with 4% paraformaldehyde. Brains were dissected out of the skull and post-fixed overnight. Sagittal or transverse 40 mm sections were cut on a vibratome (Leica 1200) and processed for free-floating immunohistochemistry. Brain sections were blocked with 10% goat or donkey serum, phosphate-buffered saline + triton (0.1% Triton X-100, PBST) and stained overnight at 4 °C with the following primary antibodies at the indicated concentrations: GFP (1:1000; ThermoFisher A-11122; Aves Lab Inc., GFP-1020), Tacr1 (1:10,000; Sigma S8305), nNOS (1:2000, Abcam Ab1376), neuropeptide Y (1:1000; Peninsula Laboratories, LLC; T-4070), parvalbumin (1:2000; SWANT; PVG-213), red fluorescent protein (RFP, 1:1000; Rockland; 600-401-379S) and somatostatin (Peninsula Laboratories, LLC; T-4547), followed by the corresponding Alexa Fluor-conjugated secondary antibodies (1:500, ThermoFisher). Sections were mounted in Fluoromount-G (SouthernBiotech) and imaged with confocal microscopy (Nikon A1R) and fluorescent microscopy (Nikon 90i). Anatomical regions were identified using the Paxinos and Allen Institute Mouse Brain Atlases.

2.3 Transmission electron microscopy

After anesthesia, adult *Tacr1*^{CreER}-ChR2-eYFP mice were transcardially perfused with 0.1M phosphate buffer (PB) pH=7.2, followed by 4% PFA and 0.5% glutaraldehyde in 0.1 M phosphate buffer (PB). Brains were post-fixed for 90 minutes in the same fixative at 4°C. Following fixation, 80 μm coronal sections were cut by vibratome in 0.1M PB and then cryoprotected with an

ascendant gradient of glycerol in 0.1M PB. The glycerol gradient involved two 30-minute incubations (10% and 20%), followed by an overnight incubation in 30% glycerol. Sections were frozen on dry ice and thawed in 0.1M PB. For the immunohistochemistry, sections were blocked with 10% normal goat serum for 1 hour at room temperature (RT), incubated overnight at $4^{O}C$ with a rabbit anti-GFP primary antibody (1:1000; ThermoFisher A-11122) in 0.1M PB, and were followed by 2 h incubation at RT in a biotinylated secondary antibody goat anti-rabbit (1:1000; Jackson Laboratories) in 0.1M PB. After, sections were incubated in avidin biotin peroxidase complex (ABC Elite; Vector Laboratories; 60 min; RT), washed in 0.1M PB and developed with 3, 3-diaminobenzidine plus nickel (DAB; Vector Laboratories Kit; 2-5 min reaction). Sections were washed in 0.1M cacodylate buffer and postfixed with 1% osmium and 1.5% potassium ferrocyanide in cacodylate buffer for 1 hr at RT after sections were dehydrated in an ascending gradient of ethanol (ETOH; 35%, 50% 70%, 85% 90%). Sections were blocked-stained with 3% uranyl acetate in 70% ETOH for 2 hr at $4^{O}C$ before the 80% ETOH. Latest steps of dehydration were performed with 100% ETOH, propylene oxide followed by infiltration with epoxy resin (EMBed-812; Electron Microscopy Science, PA USA). Sections were flatted embedded between Aclar sheets and polymerized in an oven at $60^{O}C$ for 48 hrs. Selected areas of the cortex were trimmed and mounted on epoxy blocks and cut with a Leica EM UC7 ultramicrotome. Ultrathin sections (80 nm in thickness) were collected on single slot cupper grids with formvar. Ultrathin sections were observed with a JEOL-1400 transmission electron microscope (JEOL Ltd., Akishima Tokyo, Japan) and images were captured with an Orius^{TM} SC200 CCD camera (Gatan Inc., Warrendale, PA, USA).

2.4 Stereotaxic surgery and viruses

Animals were anaesthetized with 3–5% isoflurane and maintained at 1–2% isoflurane for the duration of the procedure. Animals were placed in a stereotaxic head frame (Kopf Instruments, Model 942 Small Animal Stereotaxic Instruments) and administered a subcutaneous dose of the analgesic (buprenorphine, 0.1 mg kg^{-1}; ketoprofen, 5.0 mg kg^{-1}) at the start of the procedure and was also administered ketoprofen BID for 48 h after the procedure. The scalp was shaved, local antiseptic applied (betadine), and a midline incision made to expose the cranium. The skull was aligned using cranial fissures. Local anesthetic bupivacaine (2.5 mg kg^{-1}) was topically applied on the skull at the site of drilling. A stainless-steel burr (Fine Science Tools, 19008-07) attached to a micro drill (Foredom Electric Co., K1070 High Speed Rotary Micromotor Kit, 2.35mm Collet) was used to create a burr hole. A custom pulled 3.5" glass capillary tube (Drummond, #3-00-203-G/X replacement) was loaded with AAV. Virus was infused at a rate of 2 nL/s using a microinjector (Drummond Scientific Company, Nanoinjector III, Cat.#3-000-207) *Tacr1*^{CreER} mice were unilaterally injected with 400 nl virus. The injection needle was left in place for an additional 5 minutes and then slowly withdrawn. Viral injection was performed at the following coordinates for somatosensory cortex, barrel field (S1BF): AP, -0.60 mm; ML, ± 2.9 mm; DV: 0.5 and 0.8 mm. The skin incision was closed using 2-3 simple interrupted sutures. A small amount (< 5 ul) of 3M Vetbond was placed on top of sutures to discourage grooming-related activities at the incision site. Mice were housed with original cage-mates and given 4 weeks to recover prior to experimentation.

The following viruses were used in this study: AAVr.EF1a.DIO.hChR2(H134R).eyfp-wpre-hgh (Addgene 20298), AAV5-hSyn-Con/Foff-hChR2(h134R)-EYFP (UNC Vector Core, lot AV8475) and AAV9-CaMKIIa-hChR2(H134R)-EYFP (Addgene, 26969).

2.5 Whole tissue clearing

Whole-tissue clearing on brains from AAVrg-DIO-ChR2-YFP (Addgene 20298) injected $Tacr1^{CreER}$ mice, was performed using the CUBIC (unobstructed brain/body imaging cocktails) protocol previously described with minor modifications (Muntifering et al. 2018). Briefly, animals were transcardially perfused with 4% (PFA) and brains were post-fixed overnight. Brains were incubated in 50% CUBIC R1 solution at 37°C on a nutating shaker until brains were clear. After clearing, brains were washed with IHC buffer. Brains were then incubated in primary antibody (GFP, 1:500 ThermoFisher A-11122), washed with IHC buffer and followed with the corresponding Alexa Fluor-conjugated secondary antibodies (1:500, ThermoFisher). Brains were re-cleared in CUBIC R2 solution at 37°C on a nutating shaker until clear. Ribbon scanning microscopy of whole cortex was completed on an RS-G4 confocal microscope at a resolution of ~300 nm lateral and 2 μm axial (z-steps) using a Nikon CFI90 20x, 1.00 NA, glycerol lens. The image data was assembled using a 24-node compute cluster using custom software and analyzed using Imaris Cell Imaging Software (V9.5, Oxford Instruments).

2.6 Multiplex fluorescent in situ hybridization (FISH)

Mice were anesthetized with urethane and rapidly decapitated. The brain was quickly removed (< 2 min), placed into Tissue-Tek optimal cutting temperature (OCT) compound and flash frozen using 2-methylbutane chilled on dry ice. Tissue was kept on dry ice until cryosectioning. Cryosections (15 μm) were mounted directly onto Super Frost Plus slides, and fluorescence in situ hybridization (FISH) studies were performed according to the protocol for fresh-frozen sample susing the RNAscope Multiplex Fluorescent v1 Assay (Advanced Cell Diagnostics, ACD, 320850). Probes (Advanced Cell Diagnostics) for Mus musculus (Mm)-Tacr1 (Cat. No. 428781), Mm-tdTomato (Cat. No. 317041) Mm-Nos1 (Cat. No. 437651), Mm-Chodl (Cat. No. 450211) and Mm-Sst (Cat. No. 404631) were hybridized for 2 h at 40°C in a humidified oven, followed by rinsing in wash buffer and a series of incubations to develop the hybridized probe signal. Human prefrontal cortex (postmortem delay 2 h) was cryosectioned at 20 μm and mounted directly onto Super Frost Plus slides and FISH studies were performed according to the protocol for fresh-frozen sample using the RNAscope Multiplex Fluorescent V2 Assay (ACD, 320850). Human (Hu) probes from included Hu-TACR1 (Cat. No.17166A), Hu-NOS1 (Cat. No. 171594), Hu-CHODL (Cat. No.171634) and Hu-SST (Cat. No. 17145C). Sections were stained with DAPI (320858) and mounted with Prolong Diamond AntiFade (ThermoFisher, P36961).

2.7 Subcellular channelrhodopsin (ChR2)-assisted circuit mapping

Subcellular ChR2-assisted circuit mapping (sCRACM) was performed as previously described (Hooks et al. 2015; Petreanu et al. 2009; Hooks et al. 2013). Briefly, we obtained whole-

cell membrane potential recordings from M1 neurons in parasagittal brain slices of mice aged P42-92 containing thalamic or S1 axons expressing ChR2 and applied 1 ms blue light flashes to evoke neurotransmitter release. We pharmacologically blocked fast GABAergic synaptic transmission by applying picrotoxin (50 mM) to the extracellular solution. To prevent polysynaptic activity, we further added tetrodotoxin (TTX, 1 mM) and 4-AP (100 mM). Photon flux was always matched for 590 nm and 470nm stimuli in the same experiment. Light 585nmfrom the 590 nm LED was blocked using a bandpass filter (D607/45, Chroma). Data were acquired at 10 kHz using an Axopatch 700B (Molecular Devices) and Ephus software (www.ephus.org) on a custom-built laser scanning photostimulation microscope (Shepherd et al., 2003; Suter et al., 2010). Individual trials were repeated 5 times and averaged. Electrophysiology data were low pass filtered offline (1 kHz). Data analysis was performed with custom routines written in MATLAB (MathWorks).

2.8 Cranial window surgery

Two to four-month-old mice underwent a craniotomy involving implantation of a sterile glass window and attachment of an aluminum chamber frame (Narishige Inc., CF-10). Mice were anaesthetized with 3–5% isoflurane and maintained at 1–2% isoflurane for the duration of the craniotomy. The respiration rate and body temperature were continuously monitored throughout the procedure to ensure the appropriate level of anesthesia. A subcutaneous dose of analgesia, buprenorphine (0.1 mg kg^{-1}) and ketoprofen (5.0 mg kg^{-1}), were administered at the start of the procedure and twice a day for three additional days after the craniotomy respectively. A local anesthetic bupivacaine (2.5 mg kg^{-1}) was topically applied on skull at the site of the craniotomy.

The craniotomy was centered over the barrel cortex, approximately 1.5-2 mm posterior to bregma and 3 mm lateral to the midpoint between bregma and lambda. A custom-made cover glass consisting of a 4-mm round cover glass glued on a 5-mm round cover glass (CS-4R and CS-5R, Warner Instruments Inc.), and a chamber frame were cemented (Lang Dental Manufacturing Company, Ortho-Jet™) onto the skull. Tamoxifen administration (75 mg kg^{-1}) in *CreER* mice began 3 days post-surgery. During recovery the mice were acclimated to a custom treadmill for awake head-fixed data collection. Habituation protocol started at 15 minutes daily and increased by 15 minutes every 2 days until reaching 2 hours.

2.9 Optogenetic stimulation

Light stimulation and whisker stimulation experiments were performed in animals under awake head-fixed conditions. The light stimulus was delivered using a power-adjustable, TTL-controlled laser diode unit (CrystaLaser Inc., Reno, NV) connected to the optic fiber. The laser power at the tip of the fiber was set to 1 mW and measured using a power meter (Melles Griot 13PM001, IDEX Inc., Rochester, NY). Air puffs were delivered using a pressure injector (Toohey Spritzer, Toohey Company, Fairfield, NJ) set to 30 psi. The light stimulation parameters were selected based on previous experiments (see Extended Data).(Vazquez, Fukuda, and Kim 2018; Vazquez et al. 2014). For activation of channelrhodopsin (ChR2), a 473-nm laser delivered 30 ms light pulse at 5 Hz for 1 s every 30 s. For activation archaerhodopsin (ArchT), 589-nm laser delivered 5 ms light pulses at 5 Hz for 1 s every 30 s. At least 10 stimulation trials were collected for each stimulation parameter set. For optogenetic silencing experiments, whisker stimulation was performed before ($whisker_{initial}$) and after ($whisker_{final}$) light inhibition. Additional

experiments were conducted in a subset of mice to serve as control experiments. Control experiments were performed in *Tacr1*^{CreER} mice (ChR2 negative) and *Tacr1*^{CreER} mice expressing eYFP or GCaMP. Stimulation triggers and LDF data were recorded at 1 kHz (MP150, Biopac Systems Inc., Goleta, CA).

2.10 Laser Doppler flowmetry

A laser Doppler flowmeter (LDF; Periflux 5000/411, Perimed AB, Jarfalla, Sweden) was used to acquire CBF data evoked by light or whisker stimulation. The LDF probe used has a tip diameter of 450 mm, operating wavelength of 780 nm and a sampling rate of 1 kHz. Time series spanning 30 s were obtained from all trials starting 5 s prior to stimulation onset. The LDF time series were low-pass filtered with a rectangular cut-off of 4Hz and down-sampled to 10 Hz. An air puffer was also placed in front of the contralateral whisker pad (20-40 psi, 50 ms puffs, delivered at 5Hz). LDF was used to measure changes in cerebral blood flow (CBF). The change in CBF (ΔCBF) was calculated as CBF_{time}-$CBF_{baseline}$ / $CBF_{baseline}$ x 100. $CBF_{baseline}$ was determined as the mean CBF during the 4 s before whisker or light stimulation. Time series from all trials (10 to 12 trials) were averaged and converted to percent change for each animal and then averaged across animals. The change in maximum Δ CBF was determined as the maximum value after whisker or light stimulation. For normalized max. ΔCBF was determined as the max. ΔCBF light ON – max. ΔCBF light OFF

2.11 Two-photon microscopy

In vivo two-photon microscopy cortical imaging was performed as previously described with modifications (Iordanova et al. 2015; Vazquez, Fukuda, and Kim 2018). Awake, head-fixed mice were placed on a custom-made setup designed to accommodate light and sensory stimulation during live brain imaging. Two-photon images were acquired on (Ultima IV, Bruker Nano Inc.) coupled to an ultrafast laser (Insight X3, Newport SpectraPhysics, Inc.) tuned to a wavelength of 920 nm for studies imaging YFP/GFP/GCaMP and vasculature. Images were obtained using a 16x water immersion objective lens (0.80 NA; Nikon Inc.) with a maximum field-of-view of 800 x 800 μm. We routinely calibrate laser power output through the objective lens and use <40 mW for time series imaging. Stimulus onset (t=0) and imaging recordings were synchronized offline by identifying the frame at which the light stimulus was registered. Image acquisition was carried out using a wavelength of 920nm. Recordings with large-amplitude motion were discarded.

2.12 Vessel analysis

A subcutaneous injection of sulforhodamine 101 (SR 101, Thermo Fisher Scientific, 0.2 μl g^{-1}) was administered in mice to visualize the cerebral vasculature in vivo. We imaged arterioles and capillary branches from the middle cerebral artery. We identified a pial artery in the somatosensory cortex and traced its branching parenchymal arterioles and capillaries (cortex depth, approximately 0-500 um). To distinguish arterioles and capillaries in vivo, selection of arterioles and capillaries were guided by eYFP labeling of VSMCs ($NG2^{creER}$-GCaMP6f). Ten technical trials were acquired and averaged for each field of view. Three to seven fields of view

were acquired per imaging session. Multiple imaging sessions were collected on separate days per mouse and arteriolar and capillary dilation responses were averaged across all sessions for each mouse. To determine percent change in diameter relative to baseline, the time series were first filtered with a Gaussian filter and background subtracted with a rolling ball of 50 pixels. The change in diameter (ΔD/D) vessels was determined as ($diameter_{time}$ - $diameter_{baseline}$) /$diameter_{baseline}$. $Diameter_{baseline}$ was determined as the mean diameter during the 4 s before whisker or light stimulation. The maximum vessel dilation was determined as the maximum value before ($t < -1$ s) or after ($t > 1.5$ s) whisker or light stimulation (t = time). To determine the latency onset to dilation, a line was fitted through 80% and 20% of the maximum value. The latency onset to dilation was the time difference between the x-intercept of the line and the start of the whisker or light stimulation. In general, vessel diameters were quantified with MATLAB using full width half max of intensity profile. Time series were smoothed using the default smooth function in MATLAB (Savitzky-Golay finite impulse response, 5 points).

2.13 Calcium imaging

For determination of calcium responses in GCaMP6f labeled neurons in *Tacr*^{CreER}-GCaMP6f mice, or vascular smooth muscle cells (VSMCs) in *NG2*^{CreER}:GCaMP3 mice, a region of interest (ROI) was selected encompassing individual cells or VSMCS. Ca^{2+} transients in regions of interested were longitudinally recorded by two-photon microscopy (excitation: 920 nm). Cell morphology, distinguishable by YFP labeling, was used to unambiguously identify pericytes (vs. VSMC, oligodendrocytes) in vivo. In addition, VSMC identity was confirmed post-hoc from Z-stacks of imaging sessions based on a combination of branching order, vessel diameter and

distance from the parenchymal arteriole (Grant et al. 2019; Rungta et al. 2018). Ca^{2+} responses were quantified with MATLAB. Briefly, the change in the Ca^{2+} signal ($\Delta F/F$) was calculated as ($fluorescence_{time}$ - $fluorescence_{baseline}$)/ $fluorescence_{baseline}$. Fluorescence baseline intensity was determined as the average intensity for all time points for spontaneous activity measurements. For VSMCs, the minimum calcium response was determined as the minimum value after ($t > 1.5$ s) whisker or light stimulation. To determine latency onset to relaxation, a line was fitted through 80% and 20% of the maximum value. The latency onset to relaxation was considered the time difference between the x-intercept of the line and the start of the whisker or light stimulation. For neurons, the maximum calcium response was determined as the maximum value after ($t > 1.5$ s) whisker or light stimulation. Time series were smoothed using the customized smooth function in MATLAB (Savitzky-Golay finite impulse response, 5 points, for multiple vectors).

2.14 Statistical Analysis

All statistical analyses were performed using Prism 9 (GraphPad Software) or MATLAB (R2019a or 2020). Two group comparisons were analyzed using a two-tailed Student's *t*-test (paired or unpaired as indicated in figure legends) or non-parametric analyses. Multiple group comparisons were analyzed using a one-way ANOVA, followed by a post hoc Bonferroni analysis to correct for multiple comparisons. No data were excluded when performing statistical analysis. The s.e.m. was calculated for all experiments and displayed as errors bars in graphs. Statistical details for specific experiments (e.g., exact n values and what n represents, precision measures,

statistical tests used and definitions of significance) can be found in figure legends. Values are expressed as mean ± s.e.m. No animals were excluded from analyses.

3.0 Results

3.1 *Tacr1* marks a conserved population of long-range GABAergic neurons

Recent single-cell transcriptome analysis of cortical GABAergic neurons identified a subpopulation of somatostatin neurons that uniquely co-express *Tacr1*. Consistent with this observation, using multiplex fluorescent in situ hybridization, we discovered a small subpopulation of *Sst* neurons in the mouse cortex that uniquely co-express *Tacr1*, *Nos1* and chondrolectin (*Chodl)* (Fig. 1a-c; Extended Data Figure 1a-b) These sparse neurons are represented across all cortical layers with the highest neuron density in layer 6 and in white matter (Fig. 1b; Extended Data Fig 2a-b;). In human cortex, although the expression of *TACR1* and *NOS1* were found to be somewhat broader, we nevertheless observed the co-localization of these two markers with *CHODL* in a sparse subset of SST^{+} neurons (Figure 1d-f; Extended Data Figure 1c-d). As in mouse, this neural population was concentrated in cortical layer 6 and white matter (Figure. 1e; Extended Data Fig. 2c). As our results show that the majority of *Tacr1* neurons in mouse are quadruple labeled, co-expressing *Sst*, *Nos1* and *Chodl*, we will refer to this neuron subtype as simply *Tacr1* neurons. These findings are consistent with previous description of Tacr1 neurons in guinea pig, rat and monkey, and now we have extended this description to humans, suggesting a critical function in this neural population across species.

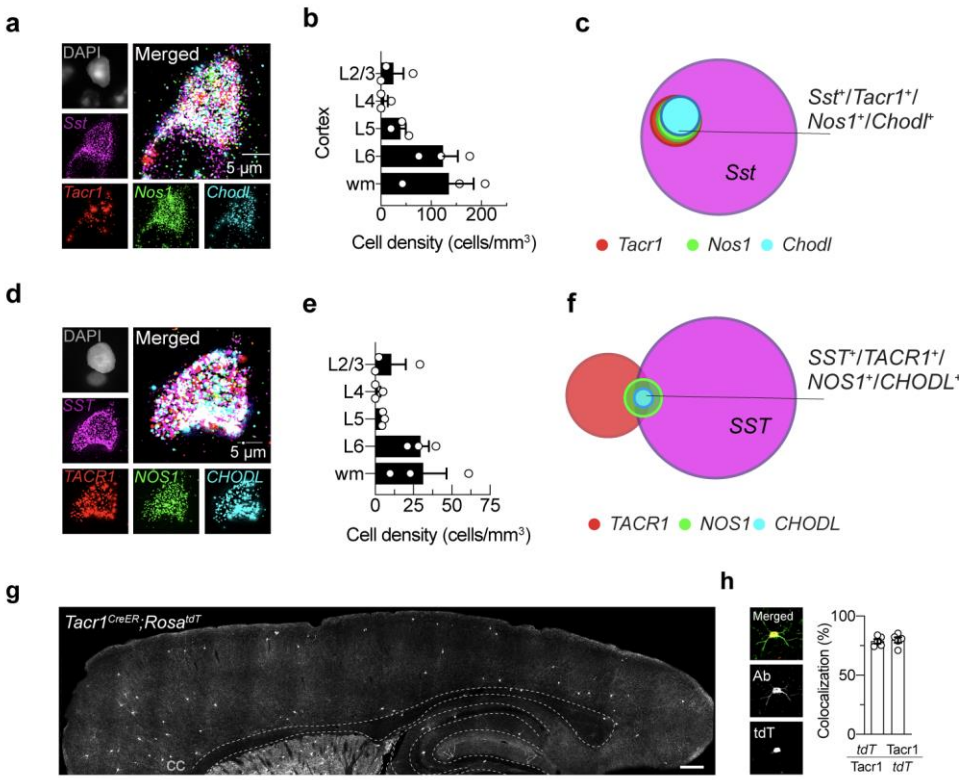

Figure 4 | *Tacr1* marks a conserved population of GABAergic neurons

a, Representative multiplex fluorescent in situ hybridization (FISH) images showing colocalization of *Sst* (purple), *Tacr1* (red), *Nos1* (green) and *Chodl* (blue) in a mouse cortical neuron (n = 3 C57BL/6). **b**, Quantification of $Sst^{+}/Tacr1^{+}/Nos1^{+}/Chodl^{+}$ neuron density in cortical and white mater (wm). **c,** Venn diagram depicting the intersectionality of neuron populations (colors correspond to those in a). Quadruple-labeled neurons represent 9.10% ± 1.99 of the *Sst* population in mouse (see Extended Data Fig. 1a). **d**, Representative multiplex FISH images showing colocalization of *SST* (purple), *TACR*1 (red), *NOS1* (green) and *CHODL* (blue) in a human cortical neuron (n = 3 human subjects). **e**., Quantification of quadruple-labeled neurons have in cortical laminae and white mater (wm). **f,** Venn diagram depicting the intersectionality of neuron populations (colors correspond to those in a). Quadruple-labeled neurons represent 1.27% ± 0.33 of the *SST* population in human (see Extended Data Fig. 1b). **g**, Representative sagittal section (left, rostral; right, caudal) of $Tacr^{1CreER}$-mediated tdTomato (*tdT*) expression in the cortex. Dashed lines are approximate anatomical borders. **h**, Representative IHC image and quantification of colocalization of *Tacr1* immunoreactivity (green) and $Tacr1^{CreER}$-mediated *tdT* expression (red) in a cortical neuron (n = 5 mice). Data are mean ± s.e.m.

We previously generated a *Tacr1*^{CreER} knock-in mouse to gain access to Tacr1 neurons in the spinal cord and the periphery, but the efficiency and specificity of *Tacr1*^{CreER}-mediated recombination within cortex is unknown. To assess the efficiency and specificity of our Cre-line in the brain, we crossed *Tacr1*^{CreER} mice to mice harboring a Cre-dependent *tdTomato* (*tdT*) fluorescent reporter expressed under control of the *Rosa* locus (Ai9 or *R26*$^{CAG\text{-}tdTomato}$) (Figure 1h). Immunohistochemistry and FISH revealed that tdT colocalization with tachykinin receptor-1 at the protein and mRNA transcript level is highly specific to *Tacr1* neurons and efficient at capturing *Tacr1*-expressing cells (Figure 1g-h; Extended Data Figure 3a-g). Using this mouse model, we demonstrate that Tacr1 neurons largely co-express *Sst*, *Nos1* and *Chodl*, aligning with our findings in wild-type mice (Extended Data Figure 4a-b).

Until recently, cortical GABAergic neurons were generally considered to be interneurons, neurons with axons projecting only a short distance from their soma. Although it's true that most GABAergic neurons have axons that reside in the same structure as their cell body, the development of viral-based anterograde and retrograde labeling, have enable the detection of a small population of GABAergic projection neurons. GABAergic projections neurons have long-range axons that project to different brain regions. There is some evidence suggesting that *Tacr1* neurons are projection neurons. To examine the projections of *Tacr1* neurons we performed viral-based retrograde labeling in combination with immunohistochemistry or whole-tissue clearing (Figure 2). We found somas of retrograde-labeled *Tacr1*^{CreER} neurons widely distributed in both ipsilateral and contralateral cortex, but unsurprisingly, a higher density in the ipsilateral side (site of viral injection). Intriguingly, somas of contralateral retrograde-labeled *Tacr1*^{CreER} neurons

dominated homotopic S1, a functionally connected region of contralateral cortex. Our findings confirm long distance (> 1.5 mm) cortico-cortical projections in this sparse *Tacr1* neurons.

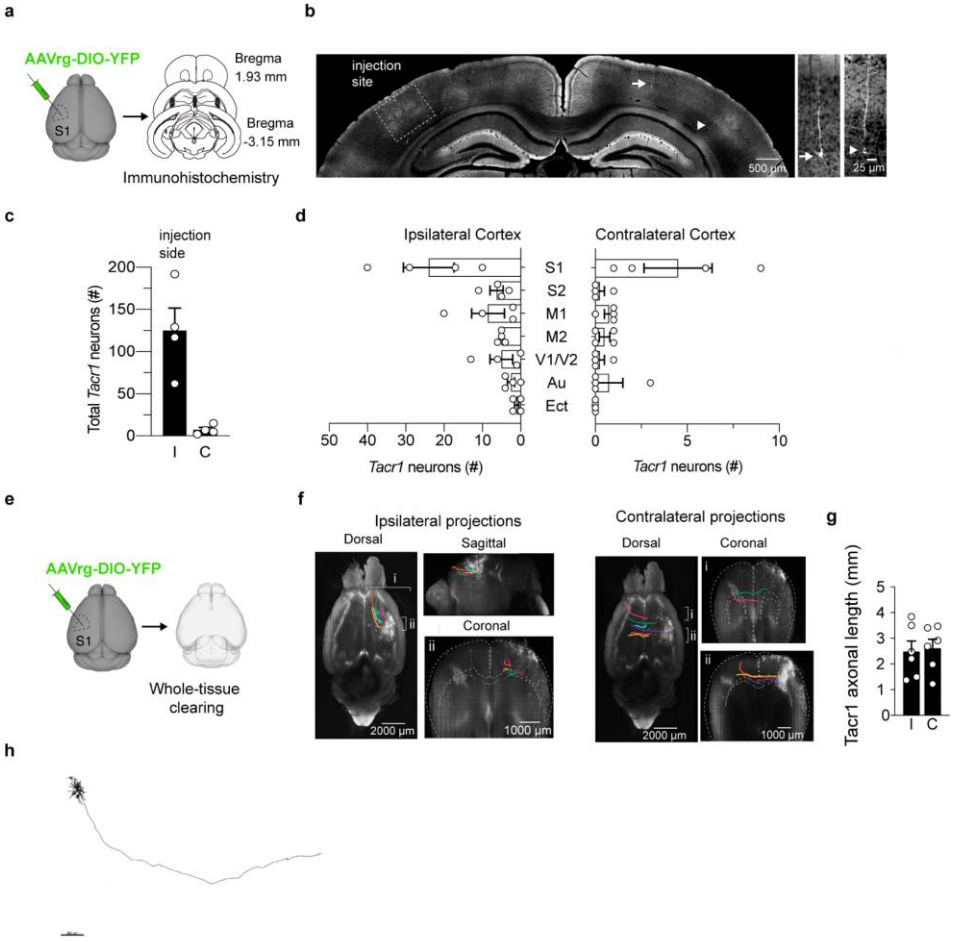

Figure 5 | Cortical Tacr1 neurons have long-range ipsilateral and contralateral projections

a, Schematic depicts viral-based AAV retrograde labeling in S1in *Tacr1*^{CreER}-tdT mice followed by IHC to evaluate cortical density and distribution of viral-labeled *Tacr1*^{CreER} soma. **b**, Representative IHC in a coronal section (dorsal aspect) demonstrating two YFP-labeled somas in the contralateral hemisphere. Enlarged YFP-labeled neurons (white arrow and arrowhead) are on the right. **c-d**, Cell density and distribution were evaluated by light microscopy (n = 4 mice). YFP-expressing Tacr1 neurons had the greatest cell density in ipsilateral S1. **e**, Schematic depicting viral-based AAV retrograde labeling in S1 *Tacr1*^{CreER} mice followed by whole-tissue clearing to evaluate long projections. **f**, Representative ipsilateral (n =5) and contralateral (n = 6) cortical *Tacr*1 long-range projections visualized by whole-tissue clearing (n = 2 mice). **g**, Ipsilateral and contralateral hemispheres had long range (> 3mm) Tacr1 projections. **h**, Example Tacr1 neuron reconstruction demonstrating long range projection Data are mean ± s.e.m.

3.2 *Tacr1* neurons are recruited in sensory-evoked NVC

The mouse whisker-to-barrel cortex pathway is a widely used model in the study of sensory-evoked neurovascular coupling. As a first step to understanding if *Tacr1* neurons play a role in NVC, we tested whether *Tacr1* neurons are involved in the sensory-evoked NVC pathway. We crossed $Tacr1^{CreER}$ mice to mice harboring a Cre-dependent GCaMP6f reporter. Using in vivo two-photon microscopy, we recorded the calcium (Ca^{2+}) signal in $Tacr1^{CreER}$ neurons during whisker stimulation (air puff; 1 s, 10 Hz, 50 psi) (Fig. 3a). We found that contralateral whisker stimulation triggered a significant Ca^{2+} elevation in *Tacr1* neurons in the barrel cortex (Fig. 3b-d). For the first time, we show that cortical *Tacr1* GABAergic neurons are recruited in the canonical circuitry of the sensory-evoked hemodynamic response. To investigate the synaptic basis of this evoked activity, we used subcellular ChR2-assisted circuit mapping (sCRACM) and found that *Tacr1* neurons receive monosynaptic cortico-cortical and thalamocortical excitatory input (Figure 3e-f). These findings provide novel insight into their connectivity and their ability to integrate local activity through feed-forward excitatory pathways.

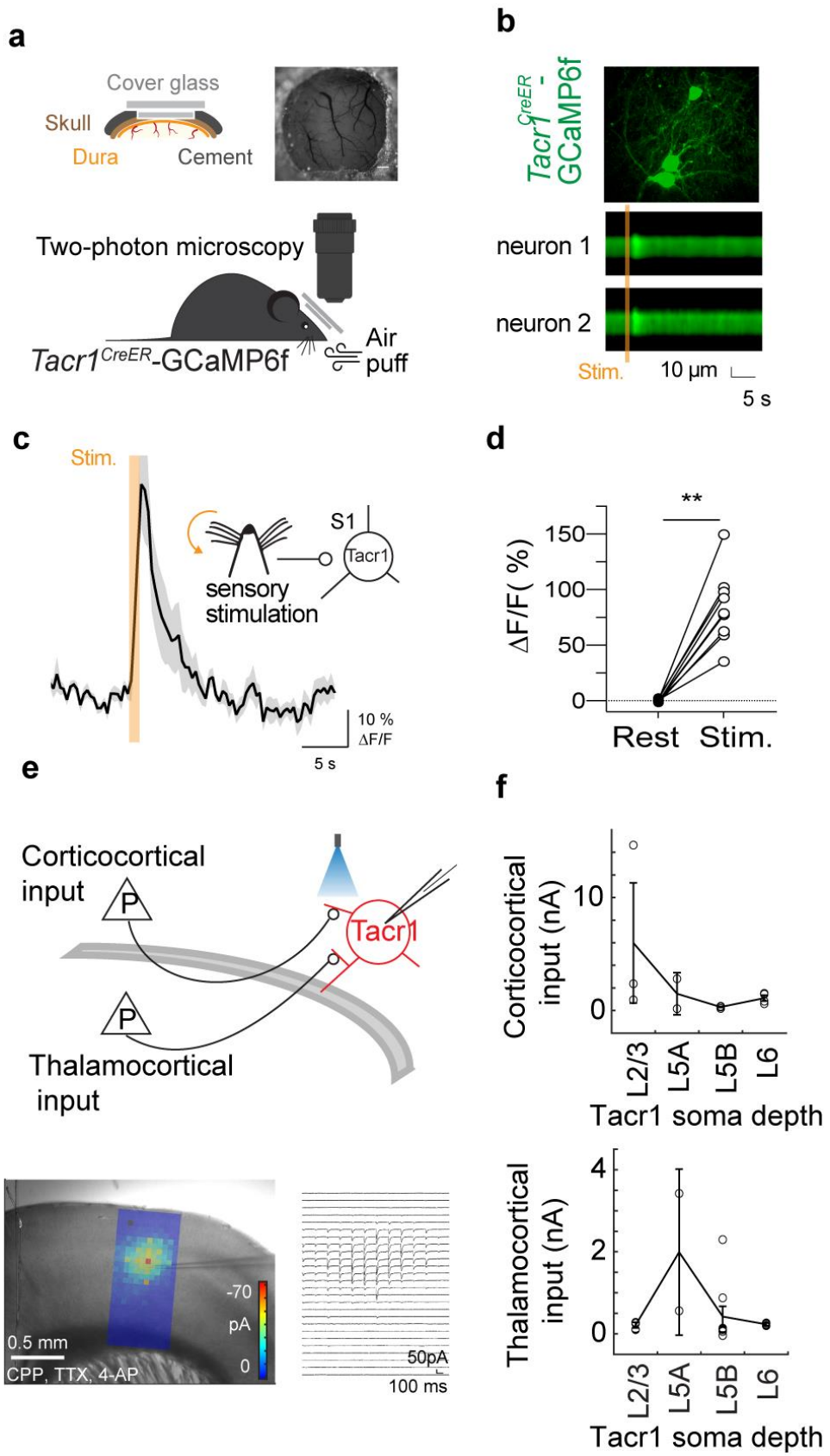
a
Cover glass
Skull
Dura
Cement
Two-photon microscopy
Tacr1CreER-GCaMP6f
Air puff
b
Tacr1CreER-GCaMP6f
neuron 1
neuron 2
Stim.
10 µm
5 s
c
Stim.
S1
Tacr1
sensory stimulation
10 %
ΔF/F
5 s
d
**
ΔF/F(%)
150
100
50
0
Rest
Stim.
e
Corticocortical input
P
Tacr1
P
Thalamocortical input
0.5 mm
CPP, TTX, 4-AP
-70
pA
0
50pA
100 ms
f
Corticocortical input (nA)
10
0
L2/3
L5A
L5B
L6
Tacr1 soma depth
Thalamocortical input (nA)
4
2
0
L2/3
L5A
L5B
L6
Tacr1 soma depth

Figure 6 | Tacr1 neurons are recruited in the cortical microcircuitry for sensory-evoked NVC

a, Top: Schematic of chronic cranial window design and representative macroscopic bright-field image of a cranial window in mouse. Bottom: Schematic depicting Ca^{2+} signal recording by two-photon microscopy in S1 cortex. Sensory stimulation (air puff) to the contralateral whisker pad was performed to evoke a hemodynamic response. **b,** Top: representative two-photon microscopy in vivo 30 μm z-stack image demonstrating GCaMP6f expression in *Tacr1*^{creER} neurons. Bottom: representative line profiles from two examples of GCaMP6f- expressing *Tacr1* neurons. Orange bar represents 1 s whisker stimulation. **c**-**d**, Time course of the percent change in Ca^{2+} signal (**c**) and maximum percent change in Ca^{2+} signal in mice expressing GCaMP6f in *Tacr1*^{creER} neurons (n = 9 neurons in 5 mice, 10 trials per neuron) before and after whisker stimulation (**d**, **P = 0.0039). **e**,Top: Schematic of subcellular ChR2-assisted circuit mapping (sCRACM) showing blue light stimulation of ChR2-expressing cortical or thalamic excitatory neurons and simultaneously recording from *tdT*-expressing *Tacr1CreER* neurons in M1. Bottom: Example sCRACM map superimposed on a brightfield image of a M1 brain slice. Responses were measured following an ~ 1 mW, 1 ms blue (473 nm) laser flash, with the laser scanned in a grid pattern (50 mm spacing, 12 x 26). **e**-**f**, Example of averaged (from 2-6 maps) excitatory postsynaptic currents ($EPSC_{sCRACM}$) recorded from a *Tacr*^{CreER}*1* neuron displayed on the grid corresponding to the light stimulus location. $EPSC_{sCRACM}$ are caused by local depolarization of ChR2-positive axons by blue light. **f**, Input vectors for M1 *Tacr1* neurons from S1. Rows of the heatmap represent individual neurons, with input summed across the same row of the map to reveal layer in which input arrived. Rows were grouped by soma depth of the postsynaptic *Tacr1* neuron. X-axis is input layer depth (in 50um bins) of S1 pyramidal neuron input. Bottom: Summed S1 input to M1 Tacr1 neurons in various cortical layers. Each oval represents a single neuron. Top: Input vectors for M1 *Tacr1* neurons from PO, plotted as in Bottom: Summed PO input to M1 Tacr1 neurons in various cortical layers, plotted at in (**e**). Statistical difference was determined by paired, nonparametric two-tailed *t*-test (**d**).

3.3 Cortical *Tacr1* neurons are required for neurovascular coupling

To test whether activation of *Tacr1* neurons is sufficient for NVC, we targeted ChR2 expression to *Tacr1* neurons. Using an in vivo laser Doppler flowmetry paradigm, we found that light activation significantly increased (by 12.87%) cerebral blood flow in ChR2-expressing mice compared to light OFF (Fig. 4a-c). Furthermore, activation of *Tacr1* neurons significantly increased CBF (by 12.50%) in $ChR2^{+}$ mice compared to $ChR2^{-}$ mice (Fig. 4d). To further address the necessity of *Tacr1* neurons in NVC, we tested whether transiently silencing cortical *Tacr1* neurons would affect the NVC response to whisker stimulation (i.e., air puff) by crossing $Tacr1^{creER}$ mice to mice with a Cre-dependent inhibitory opsin, archaerhodopsin ($R26^{LSL\text{-}ArchT\text{-}EGFP}$; ArchT). We found that light inhibition significantly decreased the whisker evoked NVC response in $ArchT^{+}$ mice during light (Fig. 4f). CBF was not significantly altered during light compared to baseline in control $ArchT^{-}$ mice (Fig 4g). The normalized CBF response was significantly different between $ArchT^{+}$ (with whisker stimulation) and $ArchT^{-}$ mice during light inhibition (Fig 4h). These experiments demonstrate that *Tacr1* neurons are critical for the a functional hemodynamic response.

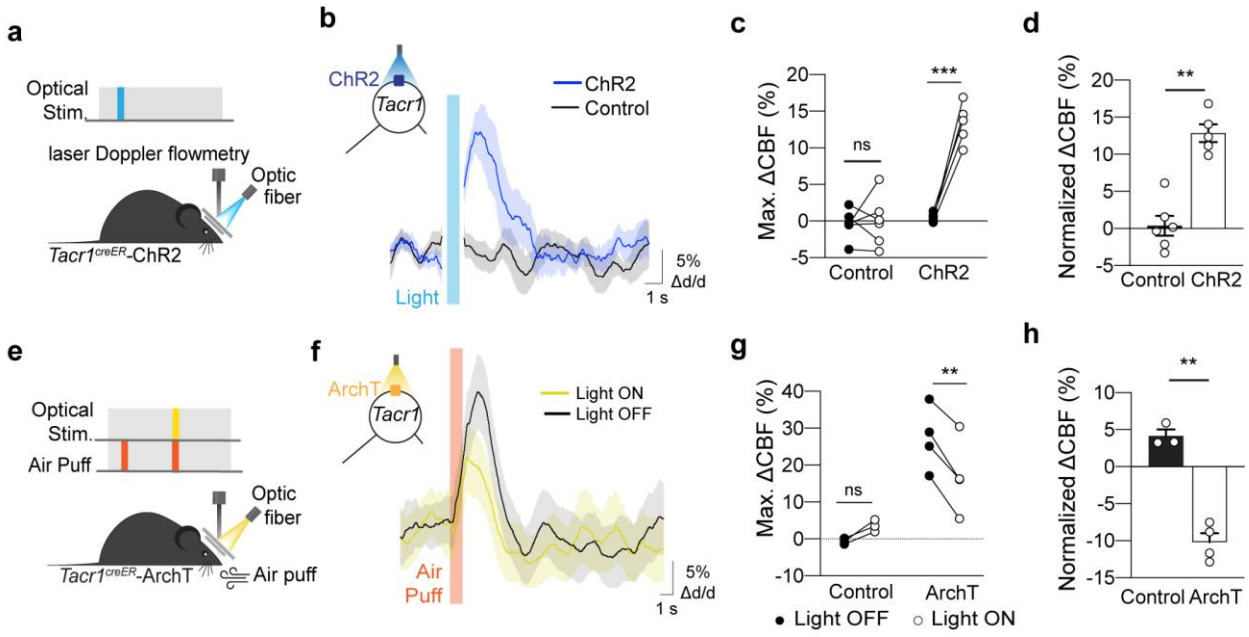

Figure 7 | Cortical *Tacr1* neurons are required for neurovascular coupling

a-d, Acute optogenetic excitation of cortical *Tacr1* neurons. **a**, Top: Optogenetic stimulation protocol (1 s, 5 Hz, 30 ms pulse width, blue light). Bottom: Experimental setup demonstrating continuous cerebral blood flow measurement by laser Doppler flowmetry (LDF) during optical excitation in awake, head-fixed mice. Blue bar represents one-second light stimulation. **b-d**, Time course of the change in CBF (**b**), maximum percent change in CBF (**c**) and normalized (to light OFF) change in CBF (**d**) in mice expressing ChR2 in *Tacr1* neurons (n=5 mice, 10 trials per mouse; solid line) relative to control mice (n = 6, 10 trials per mouse; dashed line). Activation of cortical Tacr1 neurons significantly increased CBF relative to baseline (c, ***P = 0.0004) and in control mice (d, **P = 0.0043). **e-h**, Acute optogenetic silencing of *Tacr1* neurons and simultaneous CBF recording by LDF in awake, head-fixed mice. **g**, Top: Optogenetic silencing protocol (1 s, 5 Hz, 5 ms pulse width; yellow light). Bottom: Experimental setup demonstrating continuous CBF recording by LDF during optical inhibition and/or whisker stimulation (air puff; 1 s, 10 Hz, 50 psi) in awake, head fixed mice. Orange bar represents one-second whisker stimulation. **f-h**, Time course of the change in CBF (**f**), maximum percent change in CBF (**g**, **P= 0.0038) in mice expressing ArchT in *Tacr1* neurons (n=5 mice, 10 trials per mouse) during light OFF (solid line) and light ON (dashed line). **h**, Normalized change in CBF in mice expressing ArchT in *Tacr1* neurons decreased compared to ArchT^{+} control mice (h, *P = 0.0143). Data are mean ± s.e.m. Statistical significance was determined by paired, parametric, two-tailed *t*-test (**c**, **g**) or unpaired, nonparametric two tailed *t*-test (**d, h**). ns, not significant. Error bars and shaded areas are s.e.m.

3.4 Cortical *Tacr1* neurons mediate NVC via capillary pericytes

To better understand the mechanism of cortical *Tacr1*-evoked vasodilation we hypothesized that *Tacr1* neurons mediate NVC through capillary pericytes. To test this, we investigated Ca^{2+} signal dynamics in vascular smooth muscle cells (VMSCs) in the somatosensory cortex in awake, triple transgenic *NG2*-GCaMP6;*Tacr1*^{CreER}-ChR2 mice (Fig. 5a). We found that light activation of cortical *Tacr1* neurons resulted in a decrease in the pericyte Ca^{2+} signal and subsequent vasodilation. Interestingly, the decrease in pericyte Ca^{2+} concentration (interpreted as relaxation) precedes the onset of vasodilation, suggesting that *Tacr*1-evoked pericyte relaxation triggers the hemodynamic response. Furthermore, when comparing the onset of the Ca^{2+} drop in VSMCs of parenchymal arterioles to paired pericytes enwrapping downstream capillaries (< 9 μm diameter, ranging from second-sixth order branching), we found that the decrease in the pericyte Ca^{2+} signal in pericyte preceded that of VSMCs. The finding that *Tacr1*-evoked pericyte relaxation precedes arteriolar VSMC relaxation is strengthened by the paralleled vascular response, as well as the analogous Ca^{2+} and vascular dynamics observed with sensory stimulation (Fig. 5). These findings suggest that blood flow changes evoked by Tacr1 neurons may be mediated by capillary pericytes.

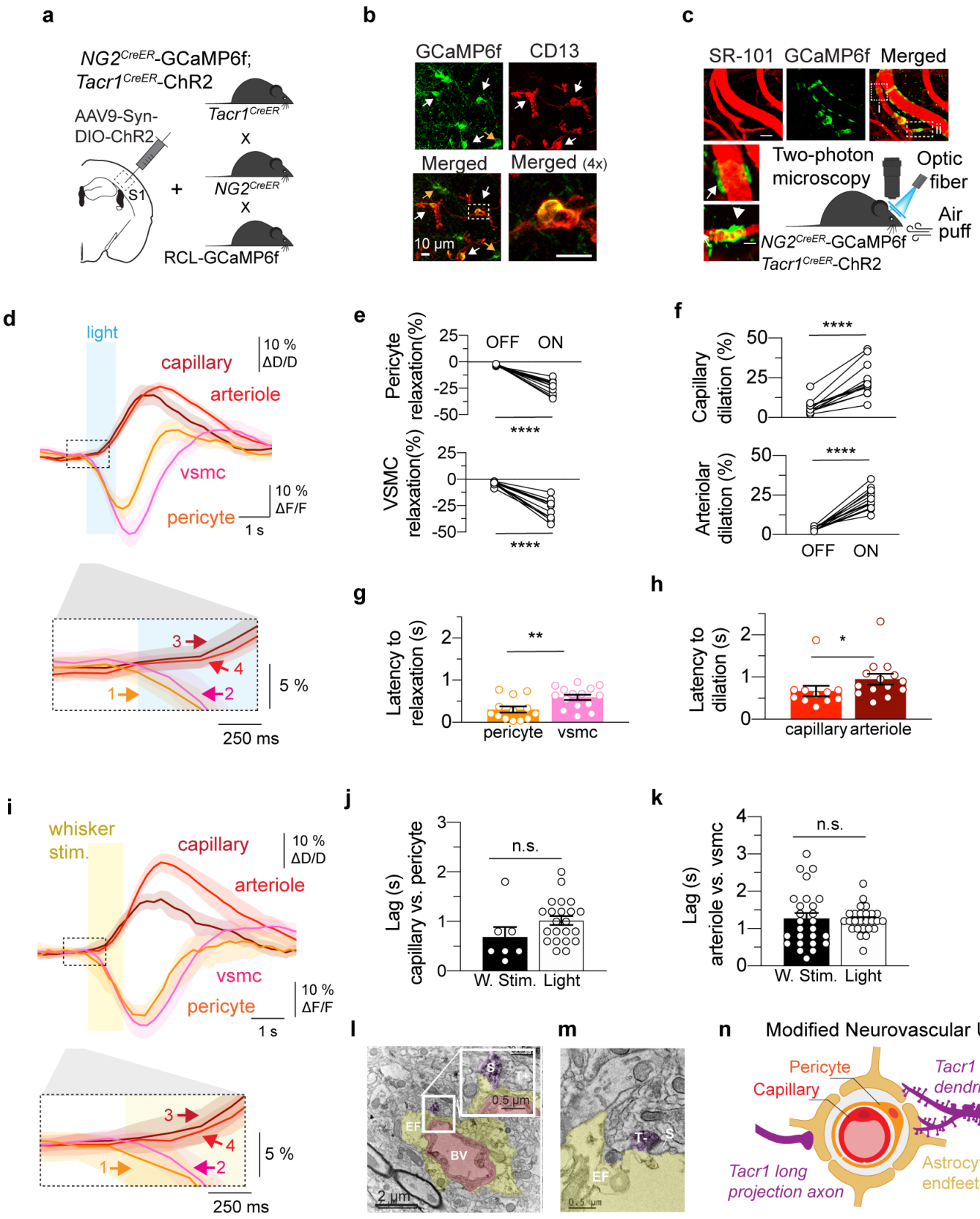
a
NG2CreER-GCaMP6f;
Tacr1CreER-ChR2
AAV9-Syn-
DIO-ChR2
S1
Tacr1CreER
X
NG2CreER
X
RCL-GCaMP6f
b
GCaMP6f
CD13
Merged
Merged (4x)
10 µm
c
SR-101
GCaMP6f
Merged
Two-photon
microscopy
Optic
fiber
Air
puff
NG2CreER-GCaMP6f
Tacr1CreER-ChR2
d
light
capillary
arteriole
vsmc
pericyte
10 %
ΔD/D
10 %
ΔF/F
1 s
3
4
1
2
5 %
250 ms
e
Pericyte
relaxation(%)
OFF
ON
****
VSMC
relaxation(%)
f
Capillary
dilation (%)
Arteriolar
dilation (%)
g
Latency to
relaxation (s)
**
pericyte
vsmc
h
Latency to
dilation (s)
*
capillary
arteriole
i
whisker
stim.
capillary
arteriole
vsmc
pericyte
10 %
ΔD/D
10 %
ΔF/F
1 s
3
4
1
2
5 %
250 ms
j
Lag (s)
capillary vs. pericyte
n.s.
W. Stim.
Light
k
Lag (s)
arteriole vs. vsmc
n.s.
W. Stim.
Light
l
S
T
0.5 µm
EF
BV
2 µm
m
T
S
EF
0.5 µm
n
Modified Neurovascular Unit
Pericyte
Capillary
Tacr1
dendrites
Tacr1 long
projection axon
Astrocyte
endfeet

Figure 8 | *Tacr1*-evoked NVC is mediated by capillary pericytes

a, Schematic depicting the generation of a triple transgenic mouse (*Tacr1*^{CreER}:*NG2*:GCaMP6f) through breeding coupled with stereotaxic injection of a Cre-dependent ChR2, synaptophysin (neuron specific) promoter AAV. **b**, White arrows indicate capillary pericytes that express GCaMP6f (green) and CD13 (pericyte marker) positive. GCaMP6f-expressing, CD13 negative cells are suspected oligodendrocytes (yellow arrow). **c**, Representative *in vivo* two-photon image showing GCaMP6f-expressing VSMCs (green) and vasculature (red). White dashed boxes in merged image shown in bottom, left. Bottom: VSMC (white arrow) on arteriole (i) and pericyte (white arrowhead) on capillary (ii). Schematic of blue light stimulation and simultaneous recording of Ca2+in VSMCs and vessel diameter. **d**-**h**, VSMCs and vascular dynamics during light stimulation in *Tacr1*^{CreER}-ChR2:*NG2*-GCaMP6f mice (n = 5 mice). **d**, Top: Time course of the change in VSMC Ca2+ signal and subsequent vessel dilation. Black dashed rectangle outlines enlarged region shown below. Bottom: At time of light stimulation VSMC relaxation precedes vascular dilation. **e**, Maximum change in pericyte (top) and VSMCs (bottom) relaxation (12 pericytes and 13 VSMCs). **f**, Maximum change in capillary (top) and arteriolar (bottom) dilation (12 capillaries and 12 arterioles). **g**-**h**, Latency to onset of VSMC relaxation or capillary dilation. **i**-**k**, VSMCs and vascular dynamics to whisker stimulation in *Tacr1*^{CreER}-ChR2;*NG2*-GCaMP6f mice (n = 5 mice). **i**, Top: Time course of the change in VSMC Ca2+ signal and subsequent vessel dilation to whisker stimulation. Black dashed lines outline an enlarged area shown at bottom. Bottom: VSMC relaxation precedes vascular dilation during light stimulation. Numbers correspond to the onset of each cell type. **j**-**k**, Lag (in seconds) determined by cross-correlation analysis between pericyte-capillary (**j**) and VSMC-arteriolar during light or whisker stimulation. l-m, Electron microscopy of *Tacr1*^{CreER} (purple) processes to the blood vessel (BV, red). BV includes endothelial cell and pericyte. **l**, Representative image of *Tacr1*^{CreER} dendritic spine (S) contacting astrocytic endfeet (EF, yellow). Inset shows a putative excitatory terminal (T+) synapsing onto the same *Tacr1*^{CreER} dendritic spine, representing a neuronal-astrocytic-vascular tripartite functional unit. **m**, The asymmetrical synapse shows *Tacr1*^{CreER} GABAergic (T-) terminal contacting astrocytic endfeet. **n**, Proposed schematic including *Tacr1* processes in in the neurovascular unit. Data are mean ± s.e.m; statistical significance was determined by paired, two-tailed *t*-test (**e**,**f**) unpaired, two-tailed Mann-Whitney test (**g**, **h**, **j**, **k**).

3.5 *Tacr1* presynaptic terminals and postsynaptic densities contact astrocytes.

Based on our Ca^{2+} imaging data, we hypothesized that *Tacr1* neural processes contact VSMCs. Using transmission electron microscopy, we found *Tacr1* presynaptic terminals and postsynaptic densities contact astrocytes. This association with the neurovascular unit demonstrates that *Tacr1* neurons are well positioned to signal to vascular elements via NO. Furthermore, the juxtaposition of an astrocytic endfoot to the symmetrical synapse between a putative excitatory presynaptic terminal and putative *Tacr1* postsynaptic densities provides evidence for glutamate-mediated postsynaptic NO release. Together *Tacr1* presynaptic and postsynaptic densities are intimately associated with the neurovascular unit and well positioned to mediate NVC.

3.6 Discussion

The main purpose of our study was to examine neurons represents the neural basis of neurovascular coupling. We discovered that a unique, genetically distinct, GABAergic neural population that expresses the tachykinin receptor 1 in both mouse and human cortex. We used sensory and light stimulation, as well as electrophysiology, to understand whether Tacr1 neurons are recruited by the whisker-to-barrel cortex hemodynamic response. Furthermore, we used light stimulation to manipulate *Tacr1* neural activity in the somatosensory cortex while simultaneously measuring VSMC activity and vascular dynamics under two-photon microscopy. We found that *Tacr1* neurons are recruited by the sensory-evoked NVC circuitry and are required for optimal feed-forward hemodynamic response. In addition, we show that *Tacr1*-evoked NVC recruits

VSMCs, either directly or indirectly. Although controversy exists regarding whether pericytes can actively dilate, our data is consistent with others and suggests that vasodilation is initiated at the capillary level. Future studies will help demonstrate whether *Tacr1*-evoked CBF response is NO dependent and if NO acts directly on smooth muscle cells / pericytes or indirectly via astrocytes. Overall, these findings provide mechanistic insight into neurovascular coupling that will help us better interpret the BOLD signal associated with diagnostic human brain imaging and advance the development of novel therapeutics that target cerebral perfusion.

.

4.0 General Discussion

4.1 Possible mechanisms for *Tacr1*-evoked vasodilation

4.1.1 Vascular smooth muscle cells

To better understand the mechanism of cortical *Tacr1*-evoked vasodilation we investigated Ca^{2+} signal dynamics in vascular smooth muscle cells in the somatosensory cortex in awake mice. Based on recent studies and the high cell density of *Tacr1* neurons in cortical layers 5 and 6, we hypothesized that *Tacr1* neurons mediate vasodilation in deep cortical layers at the level of the capillary (Uhlirova et al. 2016; Tian et al. 2010). Therefore, we hypothesized that *Tacr1*-evoked vasodilation is mediated by pericytes and found a decrease in pericyte Ca^{2+} signal, interpreted as pericyte relaxation. This drop in pericyte Ca^{2+} signal was not due to interference from the light stimulation as we observed a similar VSMC response to sensory stimulation (air puff). Interestingly, pericyte relaxation was followed by vasodilation in the associated capillary (< 9 um in diameter). These results are intriguing, but also diverge from some reports in the literature. There are several reports that capillary pericytes are passive cells and do not contribute to blood flow response induced by neural activity (Hill et al. 2015; Fernandez-Klett et al. 2010). This concept gained further acceptance based on findings from studies using novel genetic and imaging tools, as well as single-cell RNA sequencing demonstrating that pericytes do not express alpha smooth muscle actin (α-SMA), an essential protein for smooth muscle contraction (Hill et al. 2015; Vanlandewijck et al. 2018). However, other studies have concluded that pericytes can be contractile and control blood flow by regulating capillary diameter (Kisler et al. 2017). Moreover,

others have shown that pericyte loss leads to decrease CBF in health and disease (Nikolakopoulou et al. 2019; Hall et al. 2014). These conflicting reports have created controversy in the field regarding whether pericytes can actively vasodilate and modulate CBF. This confusion likely stems from the heterogeneity of smooth muscle cells, especially as vessels transition from superficial parenchymal arterioles to capillaries deep in the cortex. Classically, VSMCs are defined by their morphology as well as the vessel diameter and branch order in the vascular tree. Unfortunately, these criteria become ambiguous at various transitional points in the microcirculation, particularly at precapillary arterioles. To address this concern recent work has attempted to better define the various pericyte subtypes and put forth a classification scheme (Grant et al. 2019; Hartmann et al. 2015).

Although we defined pericytes according to the criteria in the most recent studies, we had some findings unique to *Tacr1*-evoked NVC. Previous work evaluating smooth muscle cell Ca^{2+} dynamics using a similar genetic mouse model ($NG2^{CreER}$) found a rapid, synchronous drop in the Ca^{2+} signal in all enwrapping pericytes and proximal arteriolar VSMCs to whisker stimulation (Rungta et al. 2018; Hall et al. 2014). Interestingly, the decrease in VSMC Ca^{2+} signal either coincided, or in some cases, followed the increase in RBC diameter and velocity, suggesting that the VSMCs activity was not responsible for the functional hyperemia (Rungta et al. 2018). In contrast, we found an *asynchronous* drop in the VSMC Ca^{2+} signal – the drop in pericyte Ca^{2+} signal preceded that of arteriolar VSMCs (by approximately 230 ms). This finding is strengthened by the corresponding asynchronous vascular response - capillary dilation preceded arteriolar dilation (by approximately 260 ms). Furthermore, we found *Tacr1*-evoked VSMCs calcium signal and vascular dynamics did not differ from whisker stimulation. Although Rungta et al. evaluated

the spatial-temporal dynamics of functional hyperemia in the same genetic mouse model and reporter, the different brain location (olfactory bulb vs somatosensory cortex) and stimulus (odor vs light stimulation of *Tacr1* neurons) may account for the differences. In addition, the spontaneous pericyte Ca^{2+} transients, which seem greater in magnitude in the olfactory bulb may have masked the true onset of sensory (odor)-evoked pericyte Ca^{2+} drop.

4.1.2 Astrocytes

A number of studies have reported that neurons first signal to astrocytes, which then signal to VSMCs to mediate NVC. These studies have largely focused on glutamate, released from excitatory neurons, activating metabotropic glutamate receptor 1 (mGluR1) and mGluR5 on astrocytes (Boddum et al. 2016). Glutamate binding triggers inositol triphosphate receptor (IP3-R)-associated increase in intracellular calcium concentrations in astrocytes and catalyzes the formation of prostaglandin E2 (PGE_2) and BK channels opening (Attwell et al. 2010). PGE_2 and K^+ efflux from BK channels cause smooth muscle relaxation. This signaling pathway was generally accepted, but recently the fidelity of this signaling pathway is being questioned. The work investigating glutamate signaling in astrocytes was completed in acute cortical slices in young rats, but astrocytes in adult rodents lack mGluR5s. In addition, COX1-null mice were shown to have normal NVC by laser Doppler flowmetry, although compensatory mechanisms are possible (Nizar et al. 2013). Lastly, several studies have demonstrated that various sensory stimuli, including whisker puff, foot shock and black/white drifting square gratings, do not elicit Ca^{2+} elevations in perivascular astrocytic endfeet (Nizar et al. 2013; Takata et al. 2013; Bonder and McCarthy 2014). Chemogenetic experiments have also shown that astrocytic IP3-R- dependent Ca^{2+} signaling is not necessary or sufficient for NVC in vivo (Bonder and McCarthy 2014).

Furthermore, in studies that found that sensory stimulation increases astrocytic calcium, the calcium increases do not consistently precede arteriolar dilation (Bonder and McCarthy 2014). For example, whisker stimulation in vivo induces CBF increase after approximately 600 ms, but astrocytes calcium peak two to three seconds after stimulation (Devor et al. 2003; Nizar et al. 2013). Overall, these inconsistences and temporal discrepancies suggests that astrocytes may not mediate NVC by a glutamate-driven, GCPR-linked Ca^{2+}-dependent mechanism.

4.1.2.1 A tripartite synapse

Our electron microscopy data suggests that astrocytes may mediate NVC via a different signaling pathway. We show that processes of *Tacr1* GABAergic neurons, specifically presynaptic and postsynaptic terminals, contact astrocytic endfeet. Based on our Ca^{2+} imaging data, we originally hypothesized that *Tacr1* neural processes contact VSMCs, but this may have been shortsighted considering that the CNS microvasculature is almost entirely tiled by astrocytic endfeet connected by tight junctions. Regardless, *Tacr1* terminals make direct contact with the neurovascular unit which make them well positioned to directly hyperpolarize VSMCs via NO, even when considering the diffusion kinetics of this gas (Haselden, Kedarasetti, and Drew 2020; Duchemin et al. 2012). In addition to activating VSMCs, our anatomical data suggests that cortical *Tacr1* neurons likely signal to astrocytes. The juxtaposition of an astrocytic endfoot to the symmetrical synapse between an excitatory presynaptic terminal and a *Tacr1* postsynaptic terminal is suggestive of a tripartite synapse. The tripartite synapse represents a unique synapse physiology involving the multidirectional communication between neurons and astrocytes (Perea, Navarrete, and Araque 2009; Filosa et al. 2016). It is now understood that the interactions between neurons and astrocytes is widespread and dynamic. Astrocytes' function extends beyond providing

metabolic and trophic support to neurons. Classically, a tripartite synapse consists of fine perisynaptic astrocytic processes ensheathing the synapse of a pre- and post-synaptic neuron terminal (Walker 2009; Haydon and Carmignoto 2006). It is estimated that a single mouse cortical astrocyte contacts over 100,000 synapses (Ullian et al. 2001; Dani et al. 2010). However, it is unclear whether astrocytic endfeet associated with a synapse participate in synaptic modulatory and transmission activities like the perisynaptic processes (Walker, Risher, and Risher 2020). Other reports of tripartite synapses involving astrocytic endfeet are associated with cholinergic presynaptic terminals and the dendrites of interneurons, suspected to be NO neurons (Vaucher, Linville, and Hamel 1997; Vaucher and Hamel 1995; Chedotal et al. 1994). The functional details of this complex (termed 'neuronal-astrocytic-vascular tripartite functional unit', are not completely known, but it is suspected that this interaction facilitates the release of vasoactive mediators, such as NO, to elicit a hemodynamic response. These findings align with our data and suggests that the cholinoceptive NO neurons in this report may represent *Tacr1* neurons. Altogether, it will be exciting to further dissect this unique tripartite synapse, its constituents, and its role in NVC in future studies.

4.1.2.2 NO-mediated signaling to astrocytes

The finding that Tacr1 neurons receive glutamatergic input at the neurovascular unit, or form a vasocentric tripartite synapse, is significant because NO release is mediated by glutamate (Duchemin et al. 2012). Glutamate binds to NMDA receptors on nNOS interneurons, a subpopulation that includes *Tacr1* neurons, activating nNOS (Picon-Pages, Garcia-Buendia, and Munoz 2019). nNOS is tethered to the NMDA receptor by the post-synaptic density protein-95 (PSD-95) and catalyzes the formation of NO (Christopherson et al. 1999). Conventionally, NO diffuses from post-synaptic dendrites, but EM studies have also shown that nNOS is associated

with axonal terminals as well (Aoki et al. 1993; Wang et al. 2005). Therefore, *Tacr1* neurons likely have the ability to release NO from either postsynaptic dendrites or presynaptic axonal terminals. This raises the question of which site is important for NO-mediated NVC and whether this signaling occurs indirectly via astrocyte or directly hyperpolarizes VSMCs. In astrocytes, activation of S-nitrosylation by NO has emerged as an important 'non-classical' mechanism of NO signaling (Munoz, Puebla, and Figueroa 2015). Moreover, this S-nitrosylation signaling pathway is observed close to the NO source, where NO concentration is higher (Martinez-Ruiz et al. 2013). It was shown that NO can open connexin hemichannel, such as Cx43, by S-nitrosylation, increasing intracellular Ca^{2+} (Munoz, Puebla, and Figueroa 2015). Interestingly, Cx43 is preferentially expressed on astrocytic endfeet (Simard et al. 2003). In addition to connexins, NO signaling has been shown to induce opening of BK directly by S-nitrosylation, suggesting that NO can initiate astrocytic Ca^{2+} signaling pathways.

4.1.2.3 ATP signaling to astrocytes

Lastly, *Tacr1* postsynaptic terminals may signal to astrocytic endfeet via a non-NO pathway. In general, synaptic activity evokes adenosine triphosphatase (ATP) release from post-synaptic neurons. ATP activates ATP receptors containing P2X1 subunits on astrocytes, leading to Ca^{2+} influx from the extracellular space (Mishra et al. 2016). As astrocytic endfeet are associated with a synapse involving *Tacr1* terminals, ATP from *Tacr1* postsynaptic terminals may activate astrocytic ATP receptors. Activation of astrocytic ATP receptors triggers Ca^{2+} influx and subsequent signaling cascade that leads to the formation of arachidonic acid (Mishra et al. 2016). Arachidonic acid is then metabolized, by the consecutive activity of astrocytic COX1 to produce. PGE_2. PGE_2 is thought to dilate capillaries by acting the putative EP4 receptors on pericytes. Together, the EM findings suggest that *Tacr1* terminals are well positioned to influence multiple

elements of the neurovascular unit. *Tacr1*-evoked NVC may involve glutamate-mediated, NO release from postsynaptic terminals and with subsequent signaling to VSMCs or astrocytes. In addition, *Tacr1* neurons may signal to astrocytes via a non-NO dependent mechanism, indirectly activating pericytes via a PGE_2 signaling pathway.

4.1.3 Nitric Oxide

We hypothesize that *Tacr1*-evoked vasodilation is mediated by nitric oxide. Although we did not perform pharmacology experiments to test whether *Tacr1*-evoked CBF is mitigated or blocked by a nNOS inhibitor, such as N(G)-Nitro-L-arginine methyl ester (L-NAME), the temporal dynamics of the evoked CBF is suggestive of a NO-mediated hemodynamic response. It is generally accepted that NO is an immediate early mediator of NVC, shown to account for up to 50% of the CBF response evoked by a brief (1 s) sensory stimulation (Lourenco et al. 2014; Duchemin et al. 2012). The transient and short-lived kinetics (due to the scavenging effect of hemoglobin) of NO-mediated hemodynamic response aligns with our data (Yang et al. 2005). Notably, the duration and magnitude of *Tacr1*-evoked CBF at 1 s (brief) and 4 s light stimulation is not significantly different, suggesting a fast, transient vasoactive mediator. These data are consistent with our findings that acute silencing of Tacr1 neurons mitigates but does not completely abolish the sensory-evoked NVC response.

4.2 Possible connectivity of cortical *Tacr1* neurons in sensory-evoked neurovascular coupling

4.2.1 *Tacr1* neurons and the cholinergic pathway

We found that cortical *Tacr1* neurons, a Nos1-expressing subpopulation of Sst neurons, are recruited in the sensory whisker-evoked neurovascular coupling pathway. In contrast, earlier studies using c-Fos activity mapping and double IHC found that Sst neurons are inhibited, or c-Fos negative, during whisker stimulation (Lecrux et al. 2011). Instead, cortical Sst neurons are recruited by the cholinergic and noradrenergic stimulation evoked NVC pathways. In the cholinergic-evoked NVC pathway, basal forebrain (BF)-cholinergic afferents uniquely target a small population of cortical Sst neurons that co-express Nos1 (Tong and Hamel 2000; Vaucher, Linville, and Hamel 1997). Pharmacologic and anatomical studies found that activation of these cortical Nos1 neurons via muscarinic acetylcholine (Ach) receptors, is largely responsible for the nitric oxide-mediated vasodilation in the BF-cholinergic stimulated NVC pathway (Kocharyan et al. 2008). Intriguingly, the distribution, density and co-expression of neurochemicals and neuropeptides reported in the cholinoceptive Nos1 cortical relay neurons, likely represent *Tacr1* neurons. In retrospect, the whisker-evoked *Tacr1* activity we observed in our study may be due to inadvertent co-activation of the BF-cholinergic pathway. Although the animals in our experiments are habituated to head-fixation for blood flow recording, this does not completely eliminate acute stress. A recent report evaluated cortisone concentrations in mice during head-fixation trials and found that cortisone concentrations are 2 times greater than control mice despite completing the recommended 10-day habituation protocol (Juczewski et al. 2020). Although awake head-fixation during blood flow experiments eliminates the vasoactive effects of anesthesia,

this paradigm may induce low to moderate acute stress in animals. Therefore, our findings may reflect whisker stimulation in mice with an increased Ach tone, resulting in the recruitment cortical cholinoceptive Nos1 relay neurons, or putative Tacr1 neurons, typically reserved for the BF-cholinergic NVC pathway.

However, recent in vivo pharmacology studies paired with c-Fos activity mapping showed that increased Ach tone by physostigimine or linopirdine did not alter the identity of the neuronal populations recruited, by whisker stimulation (Lecrux et al. 2017). Interestingly, in addition to COX-2 pyramidal cells and VIP interneurons, this study reported activation of a small population of cortical Sst neurons, which may represent putative *Tacr1* neurons. Therefore, this report evidence that a small population of Sst neurons are recruited during normal, physiological sensory-evoked NVC. Together, the finding of stimulus-locked increases in *Tacr1* Ca^{2+} signal demonstrate that *Tacr*1 neurons play a role in NVC. In the future evaluating the Tacr1 Ca2+ signal during whisker stimulation during altered cholinergic tone may help us better understand their role in whisker-evoked NVC pathway.

4.2.2 *Tacr1* neurons and the noradrenaline pathway

Another possible explanation for the recruitment for *Tacr1* neurons in the sensory whisker-evoked neurovascular coupling pathway is that they receive input from the locus coeruleus–noradrenalin afferents, or may be modulated by norepinephrine (Lecrux and Hamel 2016). The locus coeruleus (LC) is a brainstem nucleus that is rich in noradrenalin (NA)-containing neurons and widely innervates the cortex, targeting pyramidal neurons and GABA interneurons (Toussay

et al. 2013). Stimulation of LC evokes an increase in cortical blood and recruits both pyramidal and GABA interneurons. Interestingly, double IHC showed that at least 30% of c-Fos labeled GABA interneurons were NOS neurons. In addition, 30% of c-Fos labeled GABA interneuron were SOM, but it is unclear if the cortical NOS and SOM populations overlap (Toussay et al. 2013). Regardless, these noradrenoceptive cortical NOS neurons may represent cortical *Tacr1* neurons. As it is known that norepinephrine levels in the cortex differentially regulate functional hemodynamics in vivo, it is important to determine if the whisker stimulation triggering Ca^{2+} elevations in Tacr1 neurons represents the recruitment of these neurons in sensory-evoked NVC or is a response to norepinephrine (Bekar, Wei, and Nedergaard 2012). Reports have shown that the noise (startle) from the whisker puff can elicit an increase in cortical cerebral blood flow. As the cortex contains receives widespread noradrenergic projections from the locus coeruleus, it is likely that a norepinephrine associated CBF increase could be observed in the somatosensory cortex. Noradrenergic projections to the cortex play a prominent role in mediating startle-evoked astrocytic Ca^{2+} dynamics in fully awake mice (Ding et al., 2013; Paukert et al., 2014). Although a startle response is a concern for the observed *Tacr1* Ca^{2+} elevations, the temporal relationship between *Tacr1* Ca^{2+} activity and the blood flow response (e.g., elevation in Tacr1 Ca^{2+} signal prior to blood flow increase) suggests that a startle evoked NVC mechanism is unlikely. Startle-evoked vascular dynamics have been studied in astrocytes and show that the blood flow response precedes astrocytic Ca^{2+} elevations (Bonder and McCarthy 2014). Although the blood response suggests a sensory-evoked mechanism, it would be important to eliminate startle as a possibly for *Tacr1* activity during whisker puff in future studies.

Appendix A Extended Data

Appendix A.1 Figures

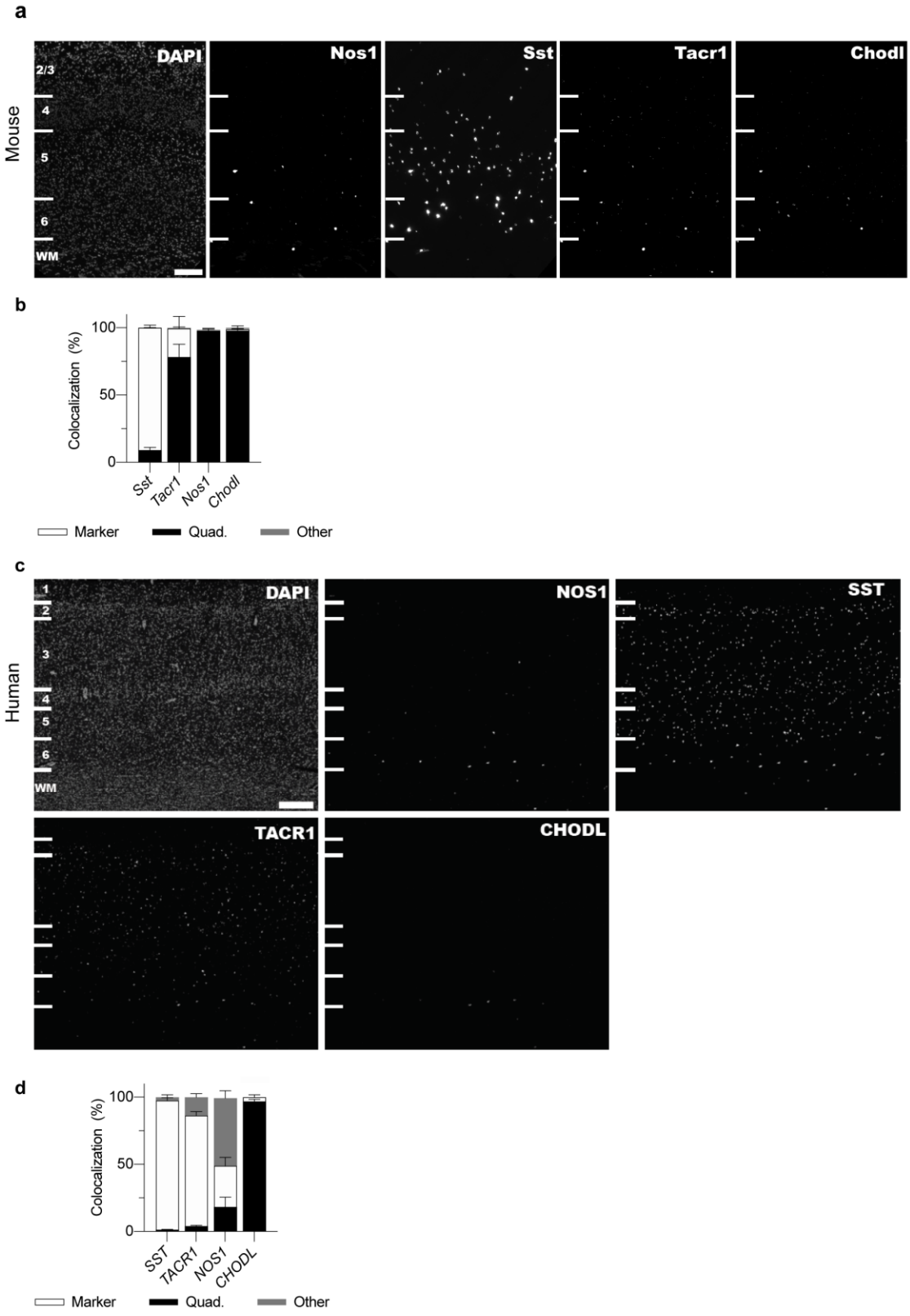
a
Mouse
DAPI
Nos1
Sst
Tacr1
Chodl
2/3
4
5
6
WM
b
Colocalization (%)
100
50
0
Sst
Tacr1
Nos1
Chodl
Marker
Quad.
Other
c
Human
DAPI
NOS1
SST
TACR1
CHODL
1
2
3
4
5
6
WM
d
Colocalization (%)
100
50
0
SST
TACR1
NOS1
CHODL
Marker
Quad.
Other

Extended Data Figure 1 | Cortical *Tacr1* neurons are largely Sst, Nos1 and Chodl positive in C57BL/6 mouse and human

a, Representative fluorescent images at low magnification of cortical section labeled for DAPI, *Nos1*, *Sst*, *Tacr1*, and *Chodl* mRNAs by multiplex FISH in wild-type mouse. Lines on the left demarcate the approximate laminar boundary, numbers indicate cortical layer. Scale bar (200 μm) in DAPI image applies to all panels. **b**, Quantification of the percent of quadruple-labeled neurons (Sst+/Tacr1+/Nos1+ /Chodl+) that make up the Sst, Tacr1, Nos1 or Chodl populations in mouse, which correspond to 9.10% ± 1.99, 78.26% ± 9.52, 97.71% ± 1.17, 97.79% ± 1.15, respectively (n = 3, C57BL/6 mice). **c**, Representative fluorescent images at low magnification of cortical section labeled for DAPI, *NOS1*, *SST*, *TACR1*, and *CHODL* mRNAs by multiplex FISH in human. Lines on the left demarcate the approximate laminar boundary, numbers indicate cortical layer. Scale bar (500 μm) in DAPI image applies to all panels. **d**, Quantification of the percent of quadruple-labeled neurons (SST^+/$TACR1^+$/$NOS1^+CHODL^+$) that comprise the *SST*, TACR1, NOS1 and CHODL populations in human which corresponds to 1.27% ± 0.33, 3.88% ± 0.63, 18.22% ± 7.34 and 96.70% ± 1.74, respectively (n = 3 human subjects). WM, white matter. Data are mean ± s.e.m.

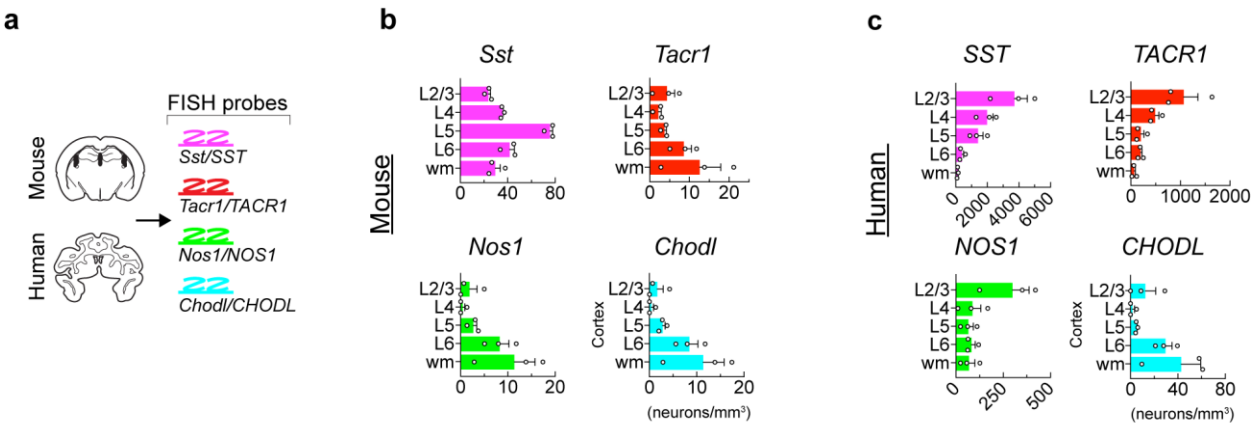

Extended Data Figure 2 | Cortical Tacr1 neurons have a similar laminar distribution in C57BL/6 mouse and human

a, Schematic of multiplex fluorescent in situ hybridization (FISH) and mRNA probes used in mouse and human cortex. **b**, Laminar distribution of somatostatin (*Sst*, purple), tachykinin receptor 1 (*Tacr1*, red), neuronal nitric oxide synthase (*Nos1*, green) and chondrolectin (*Chodl*, blue) neuron populations in mouse somatosensory cortex. **c**, Laminar distribution of *SST* (purple), *TACR1* (red), *NOS1* (green) and *CHODL* (blue) neuron populations in human prefrontal cortex.

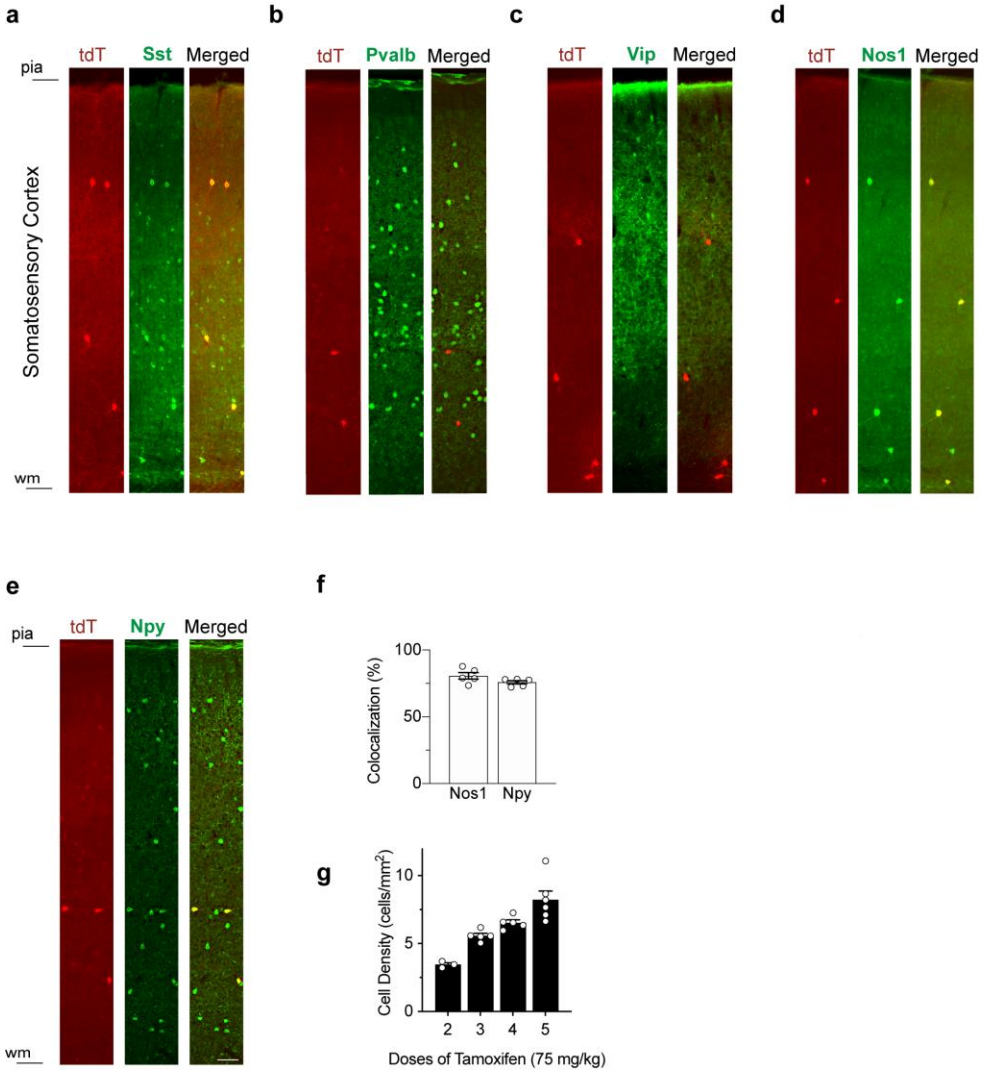

Extended Data Figure 3 | tdTomato-expressing *Tacr1* neurons largely co-express Sst, Nos1 and Npy

a-e, Representative low magnification images of immunostaining for somatostatin (Sst), parvalbumin (Pvalb), vasoactive intestinal pepetide (Vip), neuronal nitric oxide synthase (Nos1) and neuropeptide Y (Npy) in *Tacr1*^{CreER}-*tdT* mice. Scale bar, 50μm ; wm, white mater. **f**, Quantification of colocalization of tdT with Nos1 or Npy was 80.8% ± 2.48, and 75.8% ± 1.27 respectively (n = 3 Tacr1CreER-tdT mice). g, Representative merged IHC images of Tacr1CreER-mediated tdT expression and immunostaining for Sst (top), Pvalb (middle), or Vip (bottom). Quantification of tdT (red) colocalization with Sst, Pvalb, or Vip (green) was 86.4% ± 1.6, 5.9% ± 0.7, and 0.0% respectively (n = 3 mice). **h**, *Tacr1*^{CreER}-mediated recombination is dependent on the number of tamoxifen doses administered. Data are mean ± s.e.m.

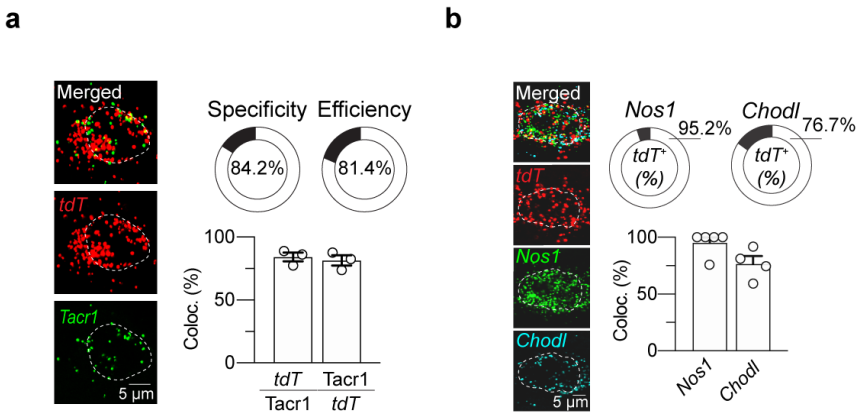

Extended Data Figure 4 | *Tacr1*^{CreER}-mediated tdTomato expression is highly specific and efficient

a, Quantification of colocalization of Tacr1 and tdT mRNA within the cortex, demonstrating high specificity (84.2% ± 3.5) and efficiency (81.4% ± 4.1). **b**, Representative multiplex FISH images of *Tacr1*^{CreER}-mediated *tdT* mRNA expression (red) colocalized with *Nos1* and *Chodl* mRNA in a cortical neuron. Quantification of the colocalization of *tdT* mRNA with *Nos1* mRNA, or *Chod*l mRNA was 95.2% ± 4.8, and 76.7% ± 6.8 respectively (n = 4 mice). Data are mean ± s.e.m. DAPI, 4′,6-diamidino-2-phenylindole; Data are mean ± s.e.m.

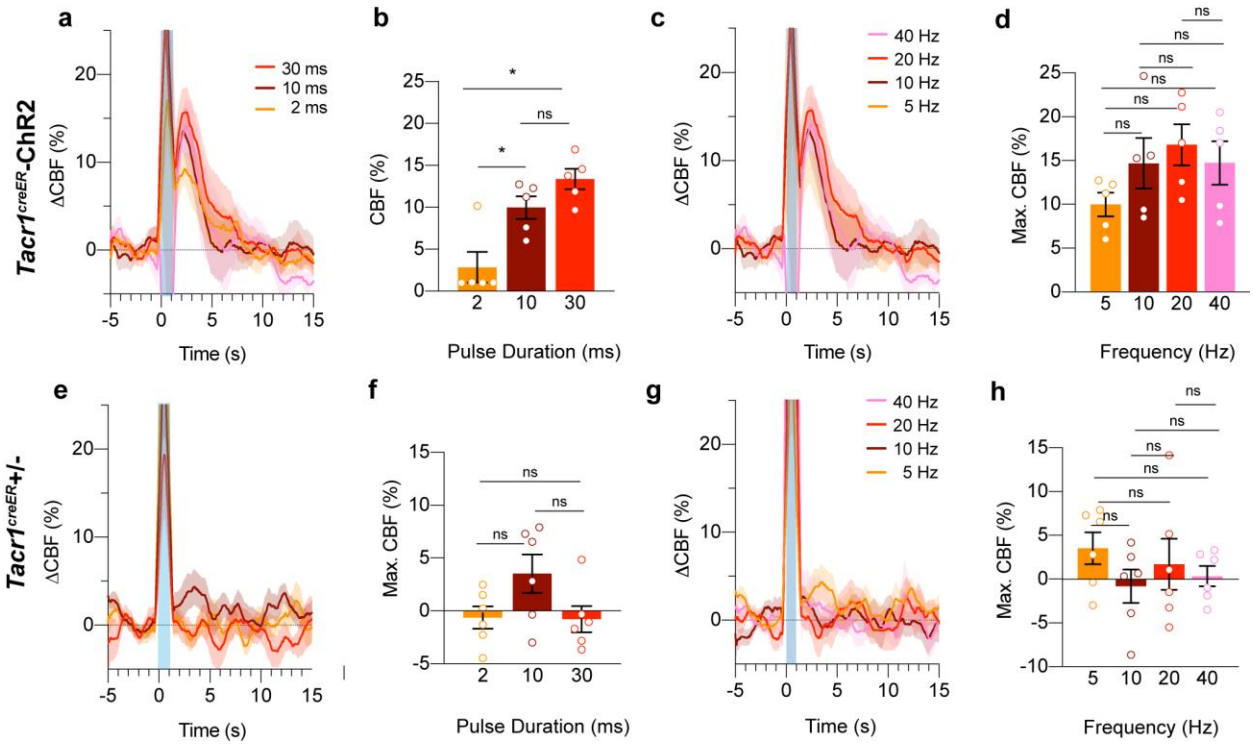

Extended Data Figure 5 | Optical excitation is dose-dependent and does not elicit a hemodynamic response in ChR2 negative mice

a-b, Optical excitation (1 s, 5 Hz) significantly increased CBF with increasing pulse duration. Time course of the change in CBF (a) and maximum percent change in CBF (b) in Tacr1creER-ChR2 mice with varied pulse duration (*P = 0.0448 for 2 ms vs. 10 ms; *P = 0.0169 for 2 ms vs 30 ms,). c-d, Optical excitation (1s, 10 ms pulse duration) with increasing frequency non-significantly increased the hemodynamics response in Tacr1creER-ChR2 mice. Time course of the change in CBF (c) and maximum percent change in CBF (d) in ChR2-expressing mice with varied optogenetic frequency. ((5 Hz, 10 Hz, 20 Hz, 40 Hz). e-h, Optical excitation does not elicit a hemodynamic response in ChR2 negative mice. Time course of the change in CBF (e) and maximum percent change in CBF (f) in Tacr1creER mice with varied pulse duration. Time course of the change in CBF (e) and maximum percent change in CBF (f) in Tacr1creER mice with varied frequency (5 Hz, 10 Hz, 20 Hz, 40 Hz). Statistical significance was determined by one-way ANOVA with a poc hoc Bonferroni multiple comparison adjustment multiple (b, d, f, h). All data are mean ± s.e.m.

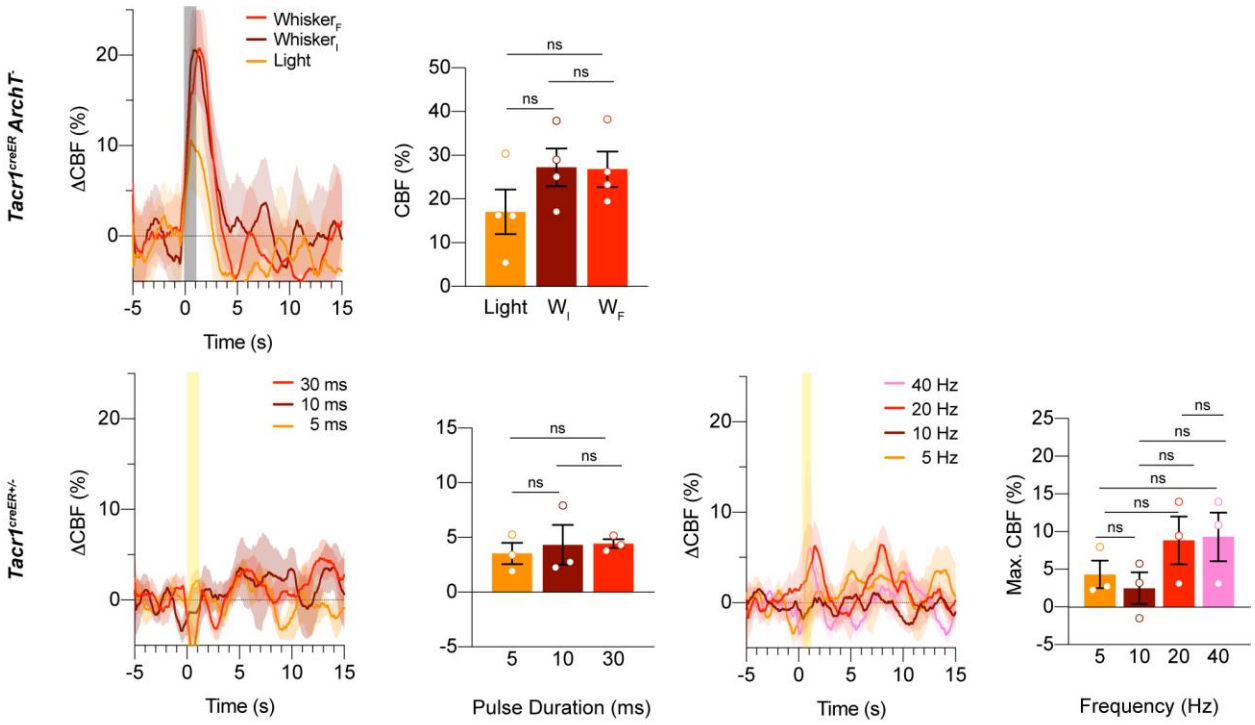

Extended Data Figure 6 | Optical inhibition did not elicit a hemodynamic response in control mice

a-**b**, Whisker response to air puff (whisker$_0$ and whisker$_1$) were not significantly different in Tacr1^{creER}-ArchT mice. **c**-**f**, Yellow light (578 nm) did not elicit a hemodynamic response in *Tacr1*^{creER} control (ArchT$^-$) mice. Time course of the change in CBF (**c**) and maximum percent change in CBF (**d**) in *Tacr1*^{creER} mice with varied pulse duration (2 ms, 10 ms, 30 ms). Yellow bar indicates period of photo-stimulation. Time course of the change in CBF (**e**) and maximum percent change in CBF (**f**) in *Tacr1*^{creER} mice with varied pulse duration (5 Hz, 10 Hz, 20 Hz, 40 Hz). Statistical significance was determined by one-way ANOVA with post hoc Bonferroni multiple comparison adjustment multiple (**b, d, f, h**). All data are mean ± s.e.m.

Bibliography

Anenberg, E., A. W. Chan, Y. Xie, J. M. LeDue, and T. H. Murphy. 2015. 'Optogenetic stimulation of GABA neurons can decrease local neuronal activity while increasing cortical blood flow', *J Cereb Blood Flow Metab*, 35: 1579-86.

Aoki, C., S. Fenstemaker, M. Lubin, and C. G. Go. 1993. 'Nitric oxide synthase in the visual cortex of monocular monkeys as revealed by light and electron microscopic immunocytochemistry', *Brain Res*, 620: 97-113.

Armstead, W. M. 2016. 'Cerebral Blood Flow Autoregulation and Dysautoregulation', *Anesthesiol Clin*, 34: 465-77.

Attwell, D., A. M. Buchan, S. Charpak, M. Lauritzen, B. A. Macvicar, and E. A. Newman. 2010. 'Glial and neuronal control of brain blood flow', *Nature*, 468: 232-43.

Bekar, L. K., H. S. Wei, and M. Nedergaard. 2012. 'The locus coeruleus-norepinephrine network optimizes coupling of cerebral blood volume with oxygen demand', *J Cereb Blood Flow Metab*, 32: 2135-45.

Boddum, K., T. P. Jensen, V. Magloire, U. Kristiansen, D. A. Rusakov, I. Pavlov, and M. C. Walker. 2016. 'Astrocytic GABA transporter activity modulates excitatory neurotransmission', *Nat Commun*, 7: 13572.

Bonder, D. E., and K. D. McCarthy. 2014. 'Astrocytic Gq-GPCR-linked IP3R-dependent Ca2+ signaling does not mediate neurovascular coupling in mouse visual cortex in vivo', *J Neurosci*, 34: 13139-50.

Carvajal, Jorge, Alfredo Germain, Juan Pablo Huidobro-Toro, and Carl Weiner. 2000. 'Molecular mechanism of cGMP-mediated smooth muscle relaxation', *Journal of Cellular Physiology*, 184: 409-20.

Cauli, B., X. K. Tong, A. Rancillac, N. Serluca, B. Lambolez, J. Rossier, and E. Hamel. 2004. 'Cortical GABA interneurons in neurovascular coupling: relays for subcortical vasoactive pathways', *J Neurosci*, 24: 8940-9.

Chedotal, Alain, Denis Umbriaco, Laurent Descarries, Boyd Hartman, and Edith Hamel. 1994. 'Light and electron microscopic immunocytochemical analysis of the neurovascular relationships of choline acetyltransferase and vasoactive intestinal polypeptide nerve terminals in the rat cerebral cortex', *THE JOURNAL OF COMPARATIVE NEUROLOGY*, 343: 57-71.

Christopherson, K. S., B. J. Hillier, W. A. Lim, and D. S. Bredt. 1999. 'PSD-95 assembles a ternary complex with the N-methyl-D-aspartic acid receptor and a bivalent neuronal NO synthase PDZ domain', *J Biol Chem*, 274: 27467-73.

Cipolla, MJ. 2009. 'Control of Cerebral Blood Flow.' in, *The Cerebral Circulation* (Moergan & Claypool Life Sciences: San Rafael).

Dani, A., B. Huang, J. Bergan, C. Dulac, and X. Zhuang. 2010. 'Superresolution imaging of chemical synapses in the brain', *Neuron*, 68: 843-56.

Devor, A., A. K. Dunn, M. L. Andermann, I. Ulbert, D. A. Boas, and A. M. Dale. 2003. 'Coupling of total hemoglobin concentration, oxygenation, and neural activity in rat somatosensory cortex', *Neuron*, 39: 353-9.

Dittrich, L., J. E. Heiss, D. R. Warrier, X. A. Perez, M. Quik, and T. S. Kilduff. 2012. 'Cortical nNOS neurons co-express the NK1 receptor and are depolarized by Substance P in multiple mammalian species', *Front Neural Circuits*, 6: 31.

Duchemin, S., M. Boily, N. Sadekova, and H. Girouard. 2012. 'The complex contribution of NOS interneurons in the physiology of cerebrovascular regulation', *Front Neural Circuits*, 6: 51.

Echagarruga, C. T., K. W. Gheres, J. N. Norwood, and P. J. Drew. 2020. 'nNOS-expressing interneurons control basal and behaviorally evoked arterial dilation in somatosensory cortex of mice', *Elife*, 9.

Fernandez-Klett, F., N. Offenhauser, U. Dirnagl, J. Priller, and U. Lindauer. 2010. 'Pericytes in capillaries are contractile in vivo, but arterioles mediate functional hyperemia in the mouse brain', *Proc Natl Acad Sci U S A*, 107: 22290-5.

Filosa, J. A., H. W. Morrison, J. A. Iddings, W. Du, and K. J. Kim. 2016. 'Beyond neurovascular coupling, role of astrocytes in the regulation of vascular tone', *Neuroscience*, 323: 96-109.

Fox, Peter T., and Marcus E. Raichle. 1986. 'Focal physiological uncoupling of cerebral blood flow and oxidative metabolism during somatosensory stimulation in human subjects', *Proc Natl Acad Sci USA*, 83: 1140-44.

Giannopoulos, S., A. H. Katsanos, G. Tsivgoulis, and R. S. Marshall. 2012. 'Statins and cerebral hemodynamics', *J Cereb Blood Flow Metab*, 32: 1973-6.

Grant, R. I., D. A. Hartmann, R. G. Underly, A. A. Berthiaume, N. R. Bhat, and A. Y. Shih. 2019. 'Organizational hierarchy and structural diversity of microvascular pericytes in adult mouse cortex', *J Cereb Blood Flow Metab*, 39: 411-25.

Hall, C. N., C. Reynell, B. Gesslein, N. B. Hamilton, A. Mishra, B. A. Sutherland, F. M. O'Farrell, A. M. Buchan, M. Lauritzen, and D. Attwell. 2014. 'Capillary pericytes regulate cerebral blood flow in health and disease', *Nature*, 508: 55-60.

Hall, John E., and Michael E. Hall. 2021a. 'Cerebral Blood Flow, Cerebrospinal Fluid, and Brain Metabolism.' in, *Guyton and Hall Textbook of Medical Physiology*.

———. 2021b. 'Overview of the Circulation: Pressure, Flow, and Resistance.' in, *Guyton and Hall Textbook of Medical Physiology* (Elsevier: Philadelphia).

Hartmann, D. A., R. G. Underly, R. I. Grant, A. N. Watson, V. Lindner, and A. Y. Shih. 2015. 'Pericyte structure and distribution in the cerebral cortex revealed by high-resolution imaging of transgenic mice', *Neurophotonics*, 2: 041402.

Haselden, W. D., R. T. Kedarasetti, and P. J. Drew. 2020. 'Spatial and temporal patterns of nitric oxide diffusion and degradation drive emergent cerebrovascular dynamics', *PLoS Comput Biol*, 16: e1008069.

Haydon, P. G., and G. Carmignoto. 2006. 'Astrocyte control of synaptic transmission and neurovascular coupling', *Physiol Rev*, 86: 1009-31.

He, M., J. Tucciarone, S. Lee, M. J. Nigro, Y. Kim, J. M. Levine, S. M. Kelly, I. Krugikov, P. Wu, Y. Chen, L. Gong, Y. Hou, P. Osten, B. Rudy, and Z. J. Huang. 2016. 'Strategies and Tools for Combinatorial Targeting of GABAergic Neurons in Mouse Cerebral Cortex', *Neuron*, 91: 1228-43.

Hill, R. A., L. Tong, P. Yuan, S. Murikinati, S. Gupta, and J. Grutzendler. 2015. 'Regional Blood Flow in the Normal and Ischemic Brain Is Controlled by Arteriolar Smooth Muscle Cell Contractility and Not by Capillary Pericytes', *Neuron*, 87: 95-110.

Hoge, Richard D., Jeff Atkinson, Brad Gill, Gerad R. Crelier, Sean Marrett, and G. Bruce Pike. 1999. 'Liner coupling between cerebral blood flow and oxygen consumption in activated human cortex', *Proc Natl Acad Sci USA*, 96: 9403-0908.

Hooks, B. M., J. Y. Lin, C. Guo, and K. Svoboda. 2015. 'Dual-channel circuit mapping reveals sensorimotor convergence in the primary motor cortex', *J Neurosci*, 35: 4418-26.

Hooks, B. M., T. Mao, D. A. Gutnisky, N. Yamawaki, K. Svoboda, and G. M. Shepherd. 2013. 'Organization of cortical and thalamic input to pyramidal neurons in mouse motor cortex', *J Neurosci*, 33: 748-60.

Huang, H., M. S. Kuzirian, X. Cai, L. M. Snyder, J. Cohen, D. H. Kaplan, and S. E. Ross. 2016. 'Generation of a NK1R-CreER knockin mouse strain to study cells involved in Neurokinin 1 Receptor signaling', *Genesis*, 54: 593-601.

Iadecola, C. 1993. 'Regulation of the cerebral microcirculation during neural activity: is nitric oxide the missing link?', *Trends Neurosci*, 16: 206-14.

———. 2017. 'The Neurovascular Unit Coming of Age: A Journey through Neurovascular Coupling in Health and Disease', *Neuron*, 96: 17-42.

Iadecola, C., A. J. Beitz, W. Renno, X. Xu, B. Mayer, and F. Zhang. 1993. 'Nitric oxide synthase-containing neural processes on large cerebral arteries and cerebral microvessels', *Brain Res*, 606: 148-55.

Iordanova, B., A. L. Vazquez, A. J. Poplawsky, M. Fukuda, and S. G. Kim. 2015. 'Neural and hemodynamic responses to optogenetic and sensory stimulation in the rat somatosensory cortex', *J Cereb Blood Flow Metab*, 35: 922-32.

Juczewski, K., J. A. Koussa, A. J. Kesner, J. O. Lee, and D. M. Lovinger. 2020. 'Stress and behavioral correlates in the head-fixed method: stress measurements, habituation dynamics, locomotion, and motor-skill learning in mice', *Sci Rep*, 10: 12245.

Kaplan, L., B. W. Chow, and C. Gu. 2020. 'Neuronal regulation of the blood-brain barrier and neurovascular coupling', *Nat Rev Neurosci*, 21: 416-32.

Kisler, K., A. R. Nelson, S. V. Rege, A. Ramanathan, Y. Wang, A. Ahuja, D. Lazic, P. S. Tsai, Z. Zhao, Y. Zhou, D. A. Boas, S. Sakadzic, and B. V. Zlokovic. 2017. 'Pericyte degeneration leads to neurovascular uncoupling and limits oxygen supply to brain', *Nat Neurosci*, 20: 406-16.

Kocharyan, A., P. Fernandes, X. K. Tong, E. Vaucher, and E. Hamel. 2008. 'Specific subtypes of cortical GABA interneurons contribute to the neurovascular coupling response to basal forebrain stimulation', *J Cereb Blood Flow Metab*, 28: 221-31.

Krawchuk, M. B., C. F. Ruff, X. Yang, S. E. Ross, and A. L. Vazquez. 2019. 'Optogenetic assessment of VIP, PV, SOM and NOS inhibitory neuron activity and cerebral blood flow regulation in mouse somato-sensory cortex', *J Cereb Blood Flow Metab*: 271678X19870105.

———. 2020. 'Optogenetic assessment of VIP, PV, SOM and NOS inhibitory neuron activity and cerebral blood flow regulation in mouse somato-sensory cortex', *J Cereb Blood Flow Metab*, 40: 1427-40.

Lacroix, A., X. Toussay, E. Anenberg, C. Lecrux, N. Ferreiros, A. Karagiannis, F. Plaisier, P. Chausson, F. Jarlier, S. A. Burgess, E. M. Hillman, I. Tegeder, T. H. Murphy, E. Hamel, and B. Cauli. 2015. 'COX-2-Derived Prostaglandin E2 Produced by Pyramidal Neurons Contributes to Neurovascular Coupling in the Rodent Cerebral Cortex', *J Neurosci*, 35: 11791-810.

Lecrux, C., and E. Hamel. 2016. 'Neuronal networks and mediators of cortical neurovascular coupling responses in normal and altered brain states', *Philos Trans R Soc Lond B Biol Sci*, 371.

Lecrux, C., C. H. Sandoe, S. Neupane, P. Kropf, X. Toussay, X. K. Tong, M. Lacalle-Aurioles, A. Shmuel, and E. Hamel. 2017. 'Impact of Altered Cholinergic Tones on the Neurovascular Coupling Response to Whisker Stimulation', *J Neurosci*, 37: 1518-31.

Lecrux, C., X. Toussay, A. Kocharyan, P. Fernandes, S. Neupane, M. Levesque, F. Plaisier, A. Shmuel, B. Cauli, and E. Hamel. 2011. 'Pyramidal neurons are "neurogenic hubs" in the neurovascular coupling response to whisker stimulation', *J Neurosci*, 31: 9836-47.

Lee, L., L. Boorman, E. Glendenning, C. Christmas, P. Sharp, P. Redgrave, O. Shabir, E. Bracci, J. Berwick, and C. Howarth. 2020. 'Key Aspects of Neurovascular Control Mediated by Specific Populations of Inhibitory Cortical Interneurons', *Cereb Cortex*, 30: 2452-64.

Lourenco, C. F., A. Ledo, R. M. Barbosa, and J. Laranjinha. 2017. 'Neurovascular-neuroenergetic coupling axis in the brain: master regulation by nitric oxide and consequences in aging and neurodegeneration', *Free Radic Biol Med*, 108: 668-82.

Lourenco, C. F., R. M. Santos, R. M. Barbosa, E. Cadenas, R. Radi, and J. Laranjinha. 2014. 'Neurovascular coupling in hippocampus is mediated via diffusion by neuronal-derived nitric oxide', *Free Radic Biol Med*, 73: 421-9.

Madisen, L., T. Mao, H. Koch, J. M. Zhuo, A. Berenyi, S. Fujisawa, Y. W. Hsu, A. J. Garcia, 3rd, X. Gu, S. Zanella, J. Kidney, H. Gu, Y. Mao, B. M. Hooks, E. S. Boyden, G. Buzsaki, J. M. Ramirez, A. R. Jones, K. Svoboda, X. Han, E. E. Turner, and H. Zeng. 2012. 'A toolbox of Cre-dependent optogenetic transgenic mice for light-induced activation and silencing', *Nat Neurosci*, 15: 793-802.

Martinez-Ruiz, A., I. M. Araujo, A. Izquierdo-Alvarez, P. Hernansanz-Agustin, S. Lamas, and J. M. Serrador. 2013. 'Specificity in S-nitrosylation: a short-range mechanism for NO signaling?', *Antioxid Redox Signal*, 19: 1220-35.

Mishra, A., J. P. Reynolds, Y. Chen, A. V. Gourine, D. A. Rusakov, and D. Attwell. 2016. 'Astrocytes mediate neurovascular signaling to capillary pericytes but not to arterioles', *Nat Neurosci*, 19: 1619-27.

Munoz, M. F., M. Puebla, and X. F. Figueroa. 2015. 'Control of the neurovascular coupling by nitric oxide-dependent regulation of astrocytic Ca(2+) signaling', *Front Cell Neurosci*, 9: 59.

Muntifering, M., D. Castranova, G. A. Gibson, E. Meyer, M. Kofron, and A. M. Watson. 2018. 'Clearing for Deep Tissue Imaging', *Curr Protoc Cytom*, 86: e38.

Nair, D. G. 2005. 'About being BOLD', *Brain Res Brain Res Rev*, 50: 229-43.

Nielsen, Alexander Norup, and Martin Lauritzen. 2001. 'Coupling and uncoupling of activity-dependent increases of neuronal activity and blood flow in rat somatosensory cortex', *J Appl Physiol* 533: 773-85.

Nikolakopoulou, A. M., A. Montagne, K. Kisler, Z. Dai, Y. Wang, M. T. Huuskonen, A. P. Sagare, D. Lazic, M. D. Sweeney, P. Kong, M. Wang, N. C. Owens, E. J. Lawson, X. Xie, Z. Zhao, and B. V. Zlokovic. 2019. 'Pericyte loss leads to circulatory failure and pleiotrophin depletion causing neuron loss', *Nat Neurosci*, 22: 1089-98.

Nizar, K., H. Uhlirova, P. Tian, P. A. Saisan, Q. Cheng, L. Reznichenko, K. L. Weldy, T. C. Steed, V. B. Sridhar, C. L. MacDonald, J. Cui, S. L. Gratiy, S. Sakadzic, D. A. Boas, T. I. Beka, G. T. Einevoll, J. Chen, E. Masliah, A. M. Dale, G. A. Silva, and A. Devor. 2013. 'In vivo stimulus-induced vasodilation occurs without IP3 receptor activation and may precede astrocytic calcium increase', *J Neurosci*, 33: 8411-22.

Perea, G., M. Navarrete, and A. Araque. 2009. 'Tripartite synapses: astrocytes process and control synaptic information', *Trends Neurosci*, 32: 421-31.

Perrenoud, Q., H. Geoffroy, B. Gauthier, A. Rancillac, F. Alfonsi, N. Kessaris, J. Rossier, T. Vitalis, and T. Gallopin. 2012. 'Characterization of Type I and Type II nNOS-Expressing Interneurons in the Barrel Cortex of Mouse', *Front Neural Circuits*, 6: 36.

Peterson, E. C., Z. Wang, and G. Britz. 2011. 'Regulation of cerebral blood flow', *Int J Vasc Med*, 2011: 823525.

Petreanu, L., T. Mao, S. M. Sternson, and K. Svoboda. 2009. 'The subcellular organization of neocortical excitatory connections', *Nature*, 457: 1142-5.

Picon-Pages, P., J. Garcia-Buendia, and F. J. Munoz. 2019. 'Functions and dysfunctions of nitric oxide in brain', *Biochim Biophys Acta Mol Basis Dis*, 1865: 1949-67.

Raichile, Marcus E. 1998. 'Behind the scences of funtional brain imaging: A historical and physiological perspective', *Proc Natl Acad Sci USA*, 95: 765-72.

Rungta, R. L., E. Chaigneau, B. F. Osmanski, and S. Charpak. 2018. 'Vascular Compartmentalization of Functional Hyperemia from the Synapse to the Pia', *Neuron*, 99: 362-75 e4.

Shen, J., D. Wang, X. Wang, S. Gupta, B. Ayloo, S. Wu, P. Prasad, Q. Xiong, J. Xia, and S. Ge. 2019. 'Neurovascular Coupling in the Dentate Gyrus Regulates Adult Hippocampal Neurogenesis', *Neuron*, 103: 878-90 e3.

Simard, Marie, Gregory Arcuino, Takahiro Takano, Qing Son Liu, and Maiken Nedergaard. 2003. 'Signaling at the gliovascular interface', *The Journal of Neuroscience*, 23: 9254-62.

Sweeney, M. D., K. Kisler, A. Montagne, A. W. Toga, and B. V. Zlokovic. 2018. 'The role of brain vasculature in neurodegenerative disorders', *Nat Neurosci*, 21: 1318-31.

Takata, N., T. Nagai, K. Ozawa, Y. Oe, K. Mikoshiba, and H. Hirase. 2013. 'Cerebral blood flow modulation by Basal forebrain or whisker stimulation can occur independently of large cytosolic Ca2+ signaling in astrocytes', *PLoS One*, 8: e66525.

Tasic, B., V. Menon, T. N. Nguyen, T. K. Kim, T. Jarsky, Z. Yao, B. Levi, L. T. Gray, S. A. Sorensen, T. Dolbeare, D. Bertagnolli, J. Goldy, N. Shapovalova, S. Parry, C. Lee, K. Smith, A. Bernard, L. Madisen, S. M. Sunkin, M. Hawrylycz, C. Koch, and H. Zeng. 2016. 'Adult mouse cortical cell taxonomy revealed by single cell transcriptomics', *Nat Neurosci*, 19: 335-46.

Tian, P., I. C. Teng, L. D. May, R. Kurz, K. Lu, M. Scadeng, E. M. Hillman, A. J. De Crespigny, H. E. D'Arceuil, J. B. Mandeville, J. J. Marota, B. R. Rosen, T. T. Liu, D. A. Boas, R. B. Buxton, A. M. Dale, and A. Devor. 2010. 'Cortical depth-specific microvascular dilation underlies laminar differences in blood oxygenation level-dependent functional MRI signal', *Proc Natl Acad Sci U S A*, 107: 15246-51.

Tong, X. K., and Edith Hamel. 2000. 'Basal forebrain nitric oxide synthase (NOS)-containg neurons project to microvessels and NOS neurons in the rat neocortex: cellular basis for cortical blood flow regulation', *European Journal of Neuroscience*, 12: 2769-80.

Toussay, X., K. Basu, B. Lacoste, and E. Hamel. 2013. 'Locus coeruleus stimulation recruits a broad cortical neuronal network and increases cortical perfusion', *J Neurosci*, 33: 3390-401.

Uhlirova, H., K. Kilic, P. Tian, M. Thunemann, M. Desjardins, P. A. Saisan, S. Sakadzic, T. V. Ness, C. Mateo, Q. Cheng, K. L. Weldy, F. Razoux, M. Vandenberghe, J. A. Cremonesi, C. G. Ferri, K. Nizar, V. B. Sridhar, T. C. Steed, M. Abashin, Y. Fainman, E. Masliah, S. Djurovic, O. A. Andreassen, G. A. Silva, D. A. Boas, D. Kleinfeld, R. B. Buxton, G. T. Einevoll, A. M. Dale, and A. Devor. 2016. 'Cell type specificity of neurovascular coupling in cerebral cortex', *Elife*, 5.

Ullian, Erik M., Stephanie K. Sapperstein, Karen S. Christopherson, and Ben A. Barres. 2001. 'Control of synapse number by glia', *Science*, 291.

Uludag, K., D. J. Dubowitz, E. J. Yoder, K. Restom, T. T. Liu, and R. B. Buxton. 2004. 'Coupling of cerebral blood flow and oxygen consumption during physiological activation and deactivation measured with fMRI', *Neuroimage*, 23: 148-55.

Vanlandewijck, M., L. He, M. A. Mae, J. Andrae, K. Ando, F. Del Gaudio, K. Nahar, T. Lebouvier, B. Lavina, L. Gouveia, Y. Sun, E. Raschperger, M. Rasanen, Y. Zarb, N. Mochizuki, A. Keller, U. Lendahl, and C. Betsholtz. 2018. 'A molecular atlas of cell types and zonation in the brain vasculature', *Nature*, 554: 475-80.

Vaucher, E., D. Linville, and E. Hamel. 1997. 'Cholinergic basal forebrain projections to nitric oxide synthase-containing neurons in the rat cerebral cortex', *Neuroscience*, 79: 827-36.

Vaucher, Elvire, and Edith Hamel. 1995. 'Cholinergic basal forebrain neurons project to cortical microvessels in the rat: electron microscopy study with anterogradely transported Phaseolus vulgaris leucoagglutinin and choline acetyltransferase immunocytochemistry', *The Journal of Neuroscience* 15: 7427-41.

Vaucher, Elvire, Xin-Kang Tong, Nathalie cholet, Sylviane Lantin, and Edith Hamel. 2000. ' GABA neurons provide a rich input to microvessels but not nitric oxide neurons in the rat cerebral cortex: A means for direct regulation of local cerebral blood flow', *Journal of Comparative Neurology*, 421: 161-71.

Vazquez, A. L., M. Fukuda, J. C. Crowley, and S. G. Kim. 2014. 'Neural and hemodynamic responses elicited by forelimb- and photo-stimulation in channelrhodopsin-2 mice: insights into the hemodynamic point spread function', *Cereb Cortex*, 24: 2908-19.

Vazquez, A. L., M. Fukuda, and S. G. Kim. 2018. 'Inhibitory Neuron Activity Contributions to Hemodynamic Responses and Metabolic Load Examined Using an Inhibitory Optogenetic Mouse Model', *Cereb Cortex*, 28: 4105-19.

Walker, C. D., W. C. Risher, and M. L. Risher. 2020. 'Regulation of Synaptic Development by Astrocyte Signaling Factors and Their Emerging Roles in Substance Abuse', *Cells*, 9.

Walker, Matthew. 2009. 'The Role of slow wave sleep in memory processing', *Journal of Clinical Sleep Medicine*, 5.

Wang, Y., X. F. Liu, K. G. Cornish, I. H. Zucker, and K. P. Patel. 2005. 'Effects of nNOS antisense in the paraventricular nucleus on blood pressure and heart rate in rats with heart failure', *Am J Physiol Heart Circ Physiol*, 288: H205-13.

Xiao, M., Q. Li, H. Feng, L. Zhang, and Y. Chen. 2017. 'Neural Vascular Mechanism for the Cerebral Blood Flow Autoregulation after Hemorrhagic Stroke', *Neural Plast*, 2017: 5819514.

Yang, J., J. W. Clark, R. M. Bryan, and C. S. Robertson. 2005. 'Mathematical modeling of the nitric oxide/cGMP pathway in the vascular smooth muscle cell', *Am J Physiol Heart Circ Physiol*, 289: H886-97.

Zhang, Y., Y. Yin, H. Li, and J. H. Gao. 2020. 'Measurement of CMRO2 and its relationship with CBF in hypoxia with an extended calibrated BOLD method', *J Cereb Blood Flow Metab*, 40: 2066-80.